Detector optimisation for future linear collider

Boruo Xu
of King's College

A dissertation submitted to the University of Cambridge
for the degree of Doctor of Philosophy

ii

Abstract

This is my abstract. To be or not to be.

Declaration

This dissertation is the result of my own work, except where explicit reference is made to the work of others, and has not been submitted for another qualification to this or any other university. This dissertation does not exceed the word limit for the respective Degree Committee.

Boruo Xu

Acknowledgements

Of the many people who deserve thanks, some are particularly prominent, such as my supervisor...

Preface

This will be my preface. Where is Wolly?

x

Contents

*"Two bags of pork scratchings are worth
a bag of gold."*
— Joris the Dutch

Chapter 1

Let's make introduction great again

"Introduction means introdcution"

— Theresa Trump

Introduction

1.1 Future Linear Colliders

Basic intro. LHC.

Next challenge

Future Options. FCC vs LC

LC options

Chapter 2

Detector and Physics at Future Linear Colliders

"ILC will be built next year"
    — Mysterious person

overall

Future linear collider

ILC

CLIC

2.1 CLIC vs ILC

Beam induced background effective collision energy

2.2 ILD vs SID

calorimeter

ECal

HCal

Muon chamber

Forward detector

Tracker

CLCI-background

Theory

2.3 Physics at LC

Tau - LC relavence tau

Double higgs

general higgs field

Lagrangian

current constraint

single higgs coupling measurement done in higgs

Double higgs measurement

The main mechanism for double Higgs production

2.4 Motivation

Photon - passage through matter. Photon electromagnetic shower

Since Higgs discovery in the LHC in 2012, Higgs

Ha there is a higgs.

We found higgs. Higgs is cool. It explains mass.

Why double higgs. Double higgs coulpling is unique to linear collider. It can revel much about the BSM models.

Generator level study has performed. ILC has done this this and that. gHHH in CLIC before

Here we do things differently. First subchannels, then extract both couplings simultaneously.

Chapter 3

Simulation and Reconstruction

"How to open a pandora box?"

— A wise Chinese

3.1 Monte Carlo Simulation

Simulation and reconstruction of events for the future Linear Colliders share common software framework. Simulated events are generated with Whizard software []. Pythia describes hadronisation and Tauola simulates correct spins of tau lepton decay products. Whizard allows events simulation without initial state radiation, and can simulate electron beam interaction. For the CLIC detector, electron beam induced background events are simulated and reconstructed. These events are superimposed on the physics process to save computational resources.

3.2 Event Reconstruction

Reconstruction software runs in Marlin framework [1], as a part of iLCSoft.

Event reconstruction contains following steps:

digitisation of calorimeter hits (simulated hits in this case), reconstruction of tracks in the tracking system using pattern recognition algorithms, and particle flow objects reconstruction with PandoraPFA

into physical objects containing a few main steps: digitisation of calorimeter hits (simulated hits in this case), reconstruction of tracks in the tracking system using pattern recognition algorithms, and particle flow objects reconstruction with PandoraPFA. For the CLIC detectors, there is an extra step of $\gamma\gamma \rightarrow \mathtt{hadrons}$ background suppression. We will discuss PandoraPFA citeThomson:2009rp,Marshall:2012ry,Marshall:2015rfa in details, where a lot work goes into, and the background suppression due to its relevance in later analysis.

3.3 Pandora

Inputs of PandoraPFA are digitised calorimeter hits and reconstructed tracks.

3.3.1 Track selection

Tracks are selected based on their topological properties, how likely they are from physical processes, and whether they are consistent with tracker resolution. Only selected tracks will be used for the subsequent reconstruction.

Using a helical fit of last 50 reconstructed hits, tracks are projected to the front of the ECal.

3.3.2 Calorimeter selection

Calorimeter hits are selected based on a series of criterion. The selected hits need to have energies above the threshold, using the conversion of a minimum ionising particle (MIP) equivalent.

Isolated hits, often originated from low energy neutrons in a hadronic shower, are difficult to associate to the correct hadronic shower. They are identified and not used in the clustering. But their energy is added in the particle flow object (PFO) creation step.

3.3.3 Clustering

The main clustering scheme used in PandoraPFA is cone clustering, for grouping calorimeter hits. Cone clustering has a specified opening angle of the seed hit. Because the direction of particle flows is largely unchanged from the originated particle, whether it is a electromagnetic shower, QCD radiation or hadronisation, these cone clusters have similar direction and energy to the originated particle.

Typically a high energy calorimeter hit will be chosen as a "seed". A cone with a specified opening angle and depth will be formed around the seed. The four-momentum of calorimeter hits sum to the cone's four-momentum. PandoraPFA will start to use projection of tracks at the ECal as seeds. When all tracks are used, the remaining hits will be used as seeds.

These cone clustering algorithms are widely used in the calorimeter in PandoraPFA, and they produce basic working objects, Clusters.

There are two standalone particle identification algorithms in PandoraPFA, muon identification and photon identification. Identified muons and photons will not participate in the clustering and re-clustering stages. Both algorithms aim to improve the clustering and the re-clustering. The photon identification and related algorithm will be discussed in details in chapter **??**.

3.3.4 Clusters Merging

Initial clustering scheme is aggressive at splitting clusters. The next step is to merge clusters base on clear topological signatures. For clusters associated to tracks (charged clusters) and clusters not associated to tracks(neutral clusters), track like segments in the calorimeter are identified.

These merging signatures include combining track segments, connecting tack segments with gaps, connecting track segment to a hadronic shower, and merging clusters when they are within close proximity.

3.3.5 Re-clustering

The clustering and cluster merging scheme work well for low energy (less than 50 GeV) jet. For a high energy jet, particles and the subsequent hadronic showers are more boosted and more likely to overlap each other. herefore, it is important to re-cluster base on the compatibility of the cluster energy and the associated track momentum. A cluster may be split into two, or two clusters maybe be re-clustered based on the track-cluster association. The re-clustering algorithm is applied iteratively to find a more correct clustering of calorimeter hits.

3.3.6 Photon identification

The neutral clusters are tested against an expected photon electromagnetic shower profile. The longitudinal shower profile for a photon cluster is required to be similar to a expected electromagnetic shower profile, with the discrepancy being smaller than a threshold.

3.3.7 Fragment removal

The late stage of the reconstruction will focus on merging low energy clusters, especially non-photon neutral clusters. These neutral clusters are likely to be fragments of charged clusters, instead of being a physical particle. The merging criterion are mostly based on the proximity and the energy comparison.

One algorithm will attempt to split up photon clusters, where each is originated from two close by photons. This will be described in details in chapter **??**.

3.3.8 Particle Flow Object Creation

Particle Flow Objects (PFOs) are created at the last step. Tracks are associated to the clusters based on the proximity. Simple but effective particle identification for electrons, muons are applied. Photon identifications have been applied at various stages of the reconstruction.

PFOs are the output of the PandoraPFA reconstruction. The four-momentum of these PFOs are used heavily for the downstream analysis. The electron, muon and photon identification are also used in physics analysis, such as one described in chapter **??**.

3.4 Suppression of $\gamma\gamma \rightarrow$ `hadrons` backgrounds

For the CLIC, as discussed in section **??**, significant $\gamma\gamma \rightarrow$ `hadrons` background is present. It is crucial to remove the beam induced background as they don't represent the underlying physics process.

Two Marlin process has been developed to suppress these background, a track selector and a PFO selector [2].

The track selector aims to remove poor quality and fake tracks. It places simple quality cut and a simple time of arrival cut. If the arrival time of the track at the front of the ECal, using the helical fit, differs more than $50\,\text{ns}$ from using a straight line fit, the track will be rejected.

The PFO selector utilise the high spatial resolution from the high granular calorimeter. PFOs from $\gamma\gamma \rightarrow$ `hadrons` often have low p_T and have a range of time. PFOs from physics processes have a range of p_T, and have time close to the brunch crossing time. These two distinctive features allow $\gamma\gamma \rightarrow$ `hadrons` background to be separated. The optimal suppression uses different p_T and time cuts for the central part of the detector, and for the forward part of the detector, and uses different cuts for photons, neutral PFOs and charged PFOs. Three configurations of these cuts are developed, namely "loose", "normal", and "tight" selections. As the name suggested, "loose" selection corresponds to a looser cut of p_T and time. The optimal configuration depends on the $\sqrt{s}$ of the collision, and the physics process to study.

The background suppression is used in analysis described in chapter 6

Chapter 4

Photon Reconstruction in PandoraPFA

"Photons have mass? I didnąŕt even know they were Catholic."
— Woody Allen

4.1 Introduction

Why photon reconstruction important.

4.2 Overview of photon reconstruction in PandoraPFA

PandoraPFA provides a framework for particle reconstruction [], as described in section **??**. In the linear collider content, it has a vast library of algorithms developed through years by many people. Each algorithm addresses one topological issue in the particle reconstruction []. The essential part of the PandoraPFA is track-cluster association and reclustering to find the best track-cluster pair. Algorithms that removes trackless clusters, such as removing muon clusters or photon clusters, would provide a clean environment for the track-cluster association, hence improving the jet energy resolution.

Photon identification in the PandoraPFA has two main mechanisms. The basic mechanism tests trackless clusters, the after track-cluster association and the reclustering processes. The second more sophisticated photon identification is performed before the track-cluster association and reclustering process. This algorithm identifies photon electromagnetic shower cores carefully in the dense jet environment.

Second mechanism improves jet energy resolution by correctly identifying photon electromagnetic shower cores and leaving a cleaner environment for the track-cluster association. However, the peripheral calorimeter hits to the shower cores may be left as fragments, and reconstructed as separate particles. This lowers the reconstructed photon completeness and makes the number of reconstructed photons a less useful physical quantity. Also, the second mechanism leaves rooms for improvement of photon separation resolution, illustrated in figure **??**.

This section presents a solution to the photon fragments issue. The introduced PandoraPFA algorithms also improves the photon separation resolution. Algorithms related to photon reconstruction, fragmental removal and photon splitting, which are written or introduced by authors, will be discussed below.

4.3 Overview of photon reconstruction algorithm

The photon reconstruction algorithm refers to the more sophisticated photon identification of the two main identification mechanisms, before the track-cluster association and reclustering process. The algorithm has the following steps: coarsely forming photon clusters, reconstructing photon candidate, photon ID test, and optional fragment removals.

4.3.1 Form photon clusters

This step finds large potential photon clusters. All calorimeter hits in the ECAL, which are not used in previous algorithms, are grouped into clusters using a cone based clustering algorithm. To find photon clusters, which do not deposit energies in the tracking system, the cone clustering algorithm is seeded with energetic hits. The parameters for the cone clustering are generous, allowing potentially two or three photons in one cluster.

4.3.2 Reconstruct photon candidates

The large photon clusters are split into smaller photon candidates, using two-dimensional shower profiles. The candidates close to a track projection are deemed as non-photons. Identifying photon candidates within a large photon cluster relies on the characteristic electromagnetic showers, in particular the transverse distribution. A energetic photon or electron hits the absorber layers of the ECAL, it initiates an electromagnetic shower, where electron pair production and bremsstrahlung produce more low-energy photons and electrons. The transverse distribution is characterised by a narrow cone, widening while the shower develops.

To view the transverse shower distribution, a two-dimensional energy deposition projection is constructed in the plane perpendicular to the direction of the cluster. figure 4.1 shows the energy deposition projection of two photons candidates. U and V axis are two arbitrary orthogonal axis in the transverse plane perpendicular to the direction of photons. Z axis shows the sum of the calorimeter hit energy in GeV. The bin size corresponds to the square ECAL cell size.
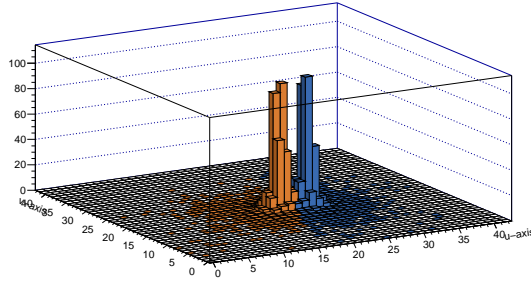
Figure 4.1: Two $500\,\text{GeV}$ photons (yellow and blue), just resolved in the transverse plane perpendicular to the direction of the flight, of their energy deposition in electromagnetic calorimeter. U and V axis are two arbitrary axis perpendicular to each other in the plane. Z axis is the sum of the calorimeter hit energy in each particular bin in 2D plane in GeV.

By using the two-dimensional energy deposition projection, separating photons translates to separating peaks in the projection. Therefore a high performance two dimensional peak finding algorithm is the key to identify multiple photons. The peak finding algorithm will be discussed in section 4.4

The output of this step is a collection of photon candidates from a photon cluster, which will be fed to the photon ID test.

4.3.3 Photon ID test

Photon ID test decides if a a candidate is a photon. If a candidate is not a photon, the calorimeter hits of the candidate will be passed on to the next stage of the reconstruction. The photon ID test is a multidimensional likelihood classifier. The classifier is trained with discriminating variables, which exploit features electromagnetic showers. The classifier will be discussed in section **??**

4.3.4 Photon Fragment removal

The optional photon fragment removal aims to merge small photon fragment to main photons. Since this step shares the same logic as the algorithm in section **??**, only differing in the cut-off values for merging metrics, this step be discussed in section **??**.

This step marks the end of the photon reconstruction algorithm. The output are a collection of reconstructed photons, separated from non-photon calorimeter hits.

4.4 Two dimensional peaking find algorithm for photon candidate

As discussed in section 4.3.2, separating photon candidates from a cluster is same as identifying peaks in a two dimensional histogram. An example of two photons is shown in the figure 4.1. The basic algorithm treats all clusters as potential photon clusters. Since charged hadrons would deposit tracks in the tracking system, extra care is taken when a cluster is close to the projection of the track in the front of the ECAL. The basic peak finding algorithm has two main functions: identifying peaks, and assigning bins to peaks.

A local peak is defined as a bin where its height is above all eight neighbouring bins. After all peak bins are found, non-peak bins are associated to one peak bin, by choosing the peak bin that minimise the metric

$$\frac{\mathrm{d}}{\sqrt{\mathrm{E}_{peak}}} \qquad\qquad (4.1)$$

where d is the Euclidean distance between a non-peak bin and a peak bin, and E_{peak} is the energy or the height of the peak bin. Alternative metrics provided in the algorithm include d, $\frac{d}{E_{peak}}$, and $\frac{d}{E_{peak}^2}$. The default metric is chosen due to a good balance between distance and energy of the peak.

4.4.1 Candidate close to track projection

If a cluster or a photon candidate is close to the projection of the track in the front of the ECAL, it is likely that the cluster or the candidate is a charged hadron. Misidentifying a charged hadron as a photon leads to significant degradation in reconstruction performance. However, if a photon next to a charged hadron is carefully reconstructed, the overall reconstruction is improved. Hence this step aims to carefully identifies photon candidate next to charged hadrons, by using track information and features of the electromagnetic shower. Photon induced electromagnetic shower in the ECAL typically start in the first few layers. As the shower develops, the direction of the shower core does not change much.

If a peak bin is within the eight neighbouring bins of the track projection onto the two dimensional plane, the peak and its associated bins are flagged as non-photons. Furthermore, the ECAL is sliced longitudinally to help identify photon candidates. For example, the default three slices will result in three ECAL fiducial spaces, each contains space from the front of the ECAL to a third, two thirds and the back of the ECAL, respectively. The peaking finding algorithm is repeated for the same cluster divided in each ECAL fiducial space. The peak is only preserved as a photon candidate if the peak exists in every fiducial space, and if its position is shifted by no more than one neighbouring bin between fiducial spaces.

4.4.2 Peak filtering

The performance of the two dimensional peaking finding algorithm is improved by clever programming and physics arguments. For a given two dimensional histogram, such as the one in figure 4.1, major peaks most likely correspond to physical photons, while the minor peaks more likely come from fluctuations in energy deposition. To select major peaks, every time after non-peak bins are associated with peak bins, minor peaks with fewer than three bins associated (including the peak bin) are discarded. These bins are then associated with non-discarded peaks. The algorithm also allows bins with height

below a critical value to not participate in the peak finding. The default value is set such that only empty bins are not used.

4.4.3 Inclusive mode

The two dimensional histogram is iterated a few times during the algorithm. The time complexity is $O(n^2)$ for a $n \times n$ histogram (Default $n = 41$). Therefore, for the purpose of speed, it is undesirable to have a very large histogram. However, since the histogram has a finite size, only energy deposition projected on the histogram would be considered for peak finding. This behaviour is suitable for photon reconstruction (section 4.3.2) and test for photon fragment removal (section 4.6). However, for photon splitting (section 4.8), there should be no calorimeter hits loss from splitting a photon. Hence inclusive mode of the peak finding algorithm is developed, and it allows energy deposition projected outside the histogram to be associated with identified peaks.

4.5 Likelihood classifier for photon ID

Section **??**

Section 4.3.3 outlines the photon ID test in the photon reconstruction algorithm. This section describes the multidimensional likelihood classifier in details, including discriminating variables. For each photon candidate, a set of kinematic variables are calculated. The classifier training typically uses simulated jet events.

Kinematic variables exploit the differences between a characteristic electromagnetic shower and a hadronic shower, and the fact that a photon is more likely to be isolated from other showers and charged tracks. Two variables use the longitudinal shower distribution: the first ECAL layer of the shower, and the difference between a expected longitudinal distribution and the observed. Two variable uses the transverse shower distribution: in the transverse plane with two orthogonal axes, the r.m.s. distance of associated bins to the peak bin, and the smallest ratio of the two r.m.s. distances in each axis direction. One variable is the ratio between the photon candidate energy to the photon cluster energy. The last kinematic variable is the distance between the photon candidate and the closest track projection. The distributions of kinematic variables are normalised to probability distribution, stored in binned histograms.

Furthermore, the classifier is improved by realising the kinematic variable distributions depend on the photon energy. Thus these distributions are divided by bins of photon candidate energy. The numbers of photon and non-photon candidates in each energy bin are also different, which helps the ID test. The default energy bins edges are 0.2, 0.5, 1, 1.5, 2.5, 5, 10, 20 GeV, which covers a good range of photon energies. Candidate with energy below 0.2 GeV would not be examined in this step, as it is very unlikely to be a photon.

For a given candidate, which falls in a energy bin, the likelihood classifier output is given by

$$\mathtt{pid} = \frac{N \prod P_i}{N \prod P_i + N' \prod P_i'} \tag{4.2}$$

where P_i and P_i' are the probability of ith kinematic variable of photon and non-photon candidates. N and N' are the number photon and non-photon candidates. These are obtained during classifier training.

During classification, a candidate passes the photon id test if

$$\begin{cases} \mathtt{pid} > 0.6, & \text{if } 0.2 < E < 0.5 \, \mathrm{GeV} \\ \mathtt{pid} > 0.4, & \text{if } E \geqslant 0.5 \, \mathrm{GeV} \end{cases} \tag{4.3}$$

where E is the candidate energy. Two values of the $\mathtt{pid}$ cuts reflect the confidence of the id test with different candidate energy. The test is more cautious with low energy candidate.

4.6 Photon fragment removal algorithm

During the reconstruction, it is possible that a core of the photon electromagnetic shower is identified as a photon (the main photon). The outer part of the shower is reconstructed as a separate particle, and wrongly identified as a photon or a neural hadron (the photon/neutral fragment). figure 4.2 shows a typical creation of such a photon fragment. The fragment does not have the electromagnetic shower structure, and typically it is has much lower energy than the main photon. If a photon-fragment pair is merged, the pair

should be consistent with a one-particle profile. These characteristics are used to merge fragments to main photons.
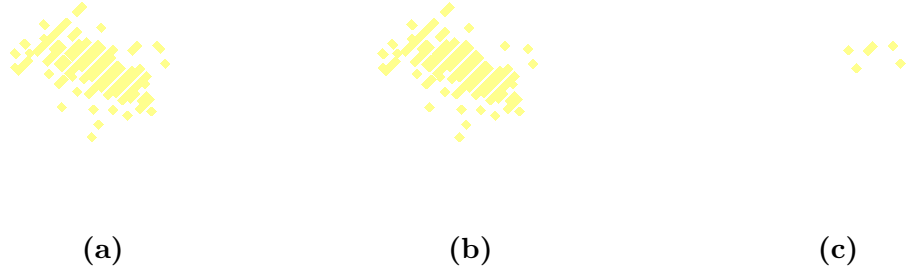

<div align="center">

(a)   **(b)**   **(c)**

</div>

Figure 4.2: An event display of a typical 10 GeV photon (figure 4.2a), reconstructed into a main photon (figure 4.2b) and a photon fragment (figure 4.2c).

Photon fragment removal algorithms can exist in multiple step in the reconstruction, at the end of the photon reconstruction (see Section 4.3.4), or at the end of the reconstruction. Since these algorithms share the same base class, the latter one will be discussed. The former differs mostly in the default cut-off values for merging metrics.

A photon and a potential fragment form a pair of particles (photon-fragment pair), if they are spatially close. Kinematic and topological properties of the photon-fragment pair are examined. The pair is merged when the properties pass a set of cuts, developed by comparing true photon-fragment pairs and non photon-fragment pair. This merging test is iterated over all possible photon-fragment pairs. If multiple photon-fragment pairs pass the merging test, the pair with closest distance metric, d, will be merged.

The photon-fragment pairs is classified into photon-photon-fragment pairs and photon-neutral-hadron-fragment pairs, because they have different kinematic and topological distributions. The pairs are further classified into low energy and high energy pair, depending on whether the fragment energy (E_p) above 1 GeV. The cuts for merging pairs, are classified which will be explained later, are listed in table 4.1.

Table 4.1 lists cuts for merging photon-photon-fragment pairs and photon-neutral-hadron-fragment pairs for both low energy and high energy fragments. d, d_c and d_h are the mean energy weighted intra-layer distance between each PFO in the pair, the distance between centroids, the minimum distance between calorimeter hits of each PFO in the pair, respectively. E_m and E_f are the main photon energy and the fragment energy. E_{p1} and E_{p2} are the two largest peaks and associated calorimeter hits, found by the two dimensional peak finding algorithm (section 4.4), ordered by descending energy, using

Low E_f	Photon-photon	Photon-neutral-hadron
transverse shower comparison	$d < 30$, $\frac{E_{p1}}{E_m+E_f} > 0.9$, $\frac{E_{p2}}{E_f} < 0.5$, $E_{p1} > E_m$	-
close proximity	-	$d < 20$, $d_c < 40$
low energy fragment	$d < 20$, $E_p < 0.4$	-
small fragment 1	$d < 30$, $N_{calo} < 40$, $d_c < 50$	$d < 50$, $N_{calo} < 10$, $d_h < 50$
small fragment 2	$d < 50$, $N_{calo} < 20$	-
small fragment forward region	$N_{calo} < 40$, $d_c < 60$, $E_f < 0.6$, $|\cos(\theta_Z)| > 0.7$	-
relative low energy fragment	$d < 40$, $d_h < 20$, $\frac{E_f}{E_m} < 0.01$	$d < 40$, $d_h < 15$, $\frac{E_f}{E_m} < 0.01$
High E_f	Photon-photon	Photon-neutral-hadron
transverse shower comparison	$\frac{E_{p1}}{E_m+E_f} > 0.9$, $E_{p2} = 0$ or $(\frac{E_{p2}}{E_f} < 0.5$, $E_{p1} > E_m)$	$\frac{E_{p1}}{E_m+E_f} > 0.9$, $E_{p2} = 0$ or $(\frac{E_{p2}}{E_f} < 0.5$, $E_{p1} > E_m)$
relative low energy fragment 1	$d < 40$, $d_h < 20$, $\frac{E_f}{E_m} < 0.02$	$d < 40$, $d_h < 20$, $\frac{E_f}{E_m} < 0.02$
relative low energy fragment 2	-	$d < 40$, $d_h < 20$, $\frac{E_f}{E_m} < 0.1$, $E_f > 10$
relative low energy fragment 3	-	$d < 20$, $d_h < 20$, $\frac{E_f}{E_m} < 0.2$, $E_f > 10$

Table 4.1: The cuts for merging photon-photon-fragment pairs and photon-neutral-hadron-fragment pairs for both low energy and high energy fragments. d, d_c and d_h are the mean energy weighted intra-layer distance of the pair, the distance between centroids, the minimum distance between calorimeter hits of the pair. E_m and E_f are the main photon energy and the fragment energy. E_{p1} and E_{p2} are the two largest peaks, found by peak finding algorithm, ordered by descending energy. N_{calo} is the number of the calorimeter hits in the fragment. $|\cos(\theta_Z)|$ is the absolute cosine of the polar angle, where beam direction is the z-axis.

the pair as input. N_{calo} is the number of the ECAL hits in the fragment. $|\cos(\theta_z)|$ is the absolute cosine of the polar angle of the main photon, where beam direction is the z-axis.

Three distance measurements have subtle difference. d_c gives the distance between centroids of each PFO in the pair, which is a quick but crude measurement. d_h is the minimum distance between calorimeter hits of each PFO in the pair. For a true photon-fragment, d_h should be close to zero as the pair should be spatially close. d is the mean energy weighted intra-layer distance between each PFO in the pair:

$$d = \frac{\sum_i^{layers} d_{l,i} \, E_{f,i}}{\sum_i^{layers} E_{f,i}} \tag{4.4}$$

where i indicates i^{th} pseudo-layer of the ECAL. $d_{l,i}$ is the minimum distance between calorimeter hits of the pair in the ith pseudo-layer. $E_{f,i}$ is the energy of the fragment in the the ith pseudo-layer. d is a better measurement of the closeness of the pair. Similar to d_h, d will be very small for a true photon-fragment pair.

One logic for merging is when the fragment is small with low energy and is close to the main photon. The other logic is when the pair looks like one photon in two-dimensional energy deposition projection (see section 4.3.2 and figure 4.1). Comparing low E_f and high E_f cut, the cuts are similar. High E_f cuts are more relaxed on the energy comparison for small fragment test. Comparing photon-photon-fragment pair and photon-neutral-hadron-pair, cuts for photon-neutral-hadron-pair are more conservative for low E_f, but more relaxed for high E_f. This reflects that the neutral hadron fragments originated from charged particles are more likely to be low energy.

Since all possible photon-fragment pairs are compared, this is a costly cooperation with $O(n^2)$ time complexity for n particles. The speed is improved by considering only the pairs with $d < 80$mm. The algorithm occurs at the end of the reconstruction.

4.7 High energy photon fragment recovery algorithm

Section 4.6 descried effective algorithms to removal photon fragments that are peripheral to the main photon, or the electromagnetic shower core. An example of such fragment is shown in figure 4.2. There is another type of fragment which is the leakage effect of the ECAL. When the high energy photon shower is not fully contained in the ECAL, shower

deposits energy in the HCAL, which often forms a neutral hadron in the HCAL. Photon reconstruction, as described in section 4.3, considers only calorimeter hits in the ECAL. An example of a 500 GeV photon reconstructed into a main photon in the ECAL (yellow) and a neutral hadron fragment in the HCAL (blue) is shown in figure 4.3. For the ILD detector, this ECAL leakage effect appears when the photon energy is above 50 GeV.
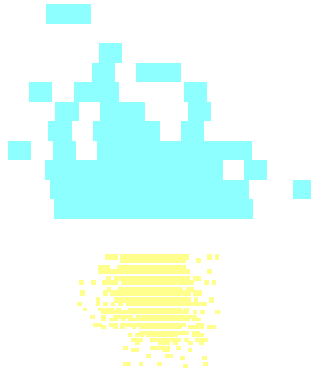

Figure 4.3: An event display of a typical 500 GeV photon, reconstructed into a main photon in the ECAL (yellow) and a neutral hadron fragment in the HCAL (blue).

With figure 4.3 as an example, high energy fragments in the HCAL is spatially close to the main photon. A fitted cone from the main photon covers most of the fragment if extended to the HCAL. These features allow a set of cuts developed to merge high energy fragments, listed in table 4.2

This algorithm would collect the photons and neutral hadrons in the HCAL as inputs. It occurs after the first pass of topological association in the reconstruction, which connects tracks to clusters in the ECAL and the HCAL. The algorithm would iterate over all pairs of reconstructed photons and neutral hadrons in the HCAL. For each pair, a set of variables are calculated and compared to a set of cuts (table 4.2). Photon-fragment pairs passing the cuts will be merged.

Fragment in the HCAL should be spatially close to the main photon, measured by three metrics. d_c^l is the distance between centroids of the last outer layer of the main photon and the first inner layer of the fragment. d_{cone}^l is the distance between fitted cones using the last outer layer of the main photon and the first inner layer of the fragment. d_{cone} is the distance between fitted cones using the main photon and the fragment.

High energy fragment recovery	Cuts
distance comparison	$d_c^l \leqslant 173$ mm, $d_{cone}^l \leqslant 100$ mm, $d_{cone} \leqslant 100$ mm
shower width comparison	$0.3 \leqslant \frac{w_f^l}{w_m^l} \leqslant 5$
projection comparison	$r_f \leqslant 45$ mm
energy comparison	$\frac{E_f}{E_m} \leqslant 0.1$
cone comparison	$\%N_{calo,cone} \geqslant 0.5$

Table 4.2: The cuts for merging high energy photon fragment in the HCAL to the main photon in the ECAL. d_c^l is the distance between centroids of the last outer layer of the main photon and the first inner layer of the fragment. d_{cone}^l is the distance between fitted cones using the last outer layer of the main photon and the first inner layer of the fragment. d_{cone} is the distance between fitted cones using the main photon and the fragment. w_m^l and w_f^l are the r.m.s. width of the last outer layer of the main photon and the first inner layer of the fragment. r_f is the r.m.s. mean energy weighted distance of a calorimeter hit in the fragment to the direction of the main photon. E_m and E_f are the main photon energy and the fragment energy. $\%N_{calo,cone}$ is the fraction of the calorimeter hits in the fragment in the extended fitted cone of the main photon.

The direction of the fragment should be similar to that of the main photon. r_f, the r.m.s. mean energy weighted distance of a calorimeter hit in the fragment to the direction of the main photon, has to be small for merging.

Another feature of the fragment and the main photon is that the shower width should be similar. w_m^l and w_f^l are the r.m.s. width of the last outer layer of the main photon and the first inner layer of the fragment. The ratio $\frac{w_f^l}{w_m^l}$ needs to be in the range of 0.3 to 5. The generous upper bound is due to the HCAL is coarser than the ECAL.

When a fitted cone from the main photon is extended to the HCAL, the cone should contain a significant amount of the fragment. $\%N_{calo,cone}$, the fraction of the calorimeter hits in the fragment in the extended fitted cone of the main photon, has to be no less than 0.5 for the merging.

The last criteria is the fragment should has low energy relative to the main photon. E_m and E_f are the main photon energy and the fragment energy. The ratio, $\frac{E_f}{E_m}$, has to be less than 0.1 for the merging.

If multiple photon-fragment pairs pass the cuts with the same fragment, the pair with highest $\%N_{calo,cone}$ will be merged.

4.8 Photon splitting algorithm

Algorithms described above deal with forming photons from calorimeter hits in the ECAL, merging photon fragments in the ECAL and the HCAL. Another aspect in photon reconstruction is splitting accidentally merged photons. During the particle reconstruction, it is possible that photons are accidentally merged if they are spatially close. Hence another algorithm at the end of the particle reconstruction addresses this issue and tries to split merged photons.

Merged photon is typically energetic. The merged photon should be consistent with topologies of a spatially closed photon pair. Extra care should be taken if the photon is close to a charged PFO. Many PandoraPFA algorithms deal with track clusters association and there is a greater confidence in clusters associated with tracks. These features form logics behind the algorithm.

Photon splitting	Cuts
Cuts	$E > E_{c1}$, $E_{p2} > E_{c2}$, $N_p < 5$
E_{c1} and E_{c2} values	
0 nearby charged PFO	$E_{c1} = 10$, $E_{c2} = 1$
1 nearby charged PFO	$E_{c1} = 10$, $E_{c2} = 5$
> 1 nearby charged PFO	$E_{c1} = 20$, $E_{c2} = 10$

Table 4.3: The cuts for splitting photons, and the values for energy cut-off points. E is the photon energy. E_{p2} is energy if the second largest peak from the two dimensional peak finding. N_p is the number of peaks identified by the peak finding. E_{c1} and E_{c2} are the energy cut-off values, determined by the number of nearby charged PFOs.

The table 4.3 shows values for the splitting a photon. E is the photon energy. E_{p2} is energy if the second largest peak from the two dimensional peak finding. N_p is the number of peaks identified by the peak finding. E_{c1} and E_{c2} are the energy cut-off values, determined by the number of nearby charged PFOs. When a energetic photon is identified, and a energetic second peak can be found by the peak finding, the photon is likely from a photon pair. N_p cut is because a reconstructed photon is unlikely from more than four photons. The values of E_{c1} and E_{c2} allow more conservative approach when a photon is close to charged PFOs.

4.9 Photon reconstruction performance

Motivations and implementations of four different algorithms for photon reconstruction, fragment removal and photon splitting have been described in the above. The main photon reconstruction algorithm in section 4.3 improves the photon completeness and the photon pair resolution, due to the improved two dimensional peak finding algorithm in section 4.4. The fragment removal algorithms in section 4.6 and section 4.7 further reduce the photon fragments in the ECAL and the HCAL. The photon splitting algorithm in section 4.8 exploits the peak finding algorithms and improves the photon separation resolution. Because of the high photon reconstruction completeness, the jet energy resolution receives a small improvement.

This section reviews the performance improvement with the introduced algorithms, using single photon, photon pair and jet samples. The performance was compared using PandoraPFA version 1 and version 3, where the photon algorithms were introduced in PandoraPFA version 2. The ILD detector model is used. The ECAL square cell size is about 5 mm. The events selected such that there is no early photon conversion and the monte carlo photon deposits energies in the calorimeter. The photon pair simulated events were generated with a uniform distribution in the solid angle for a range of the opening angles between the pair.

4.9.1 Single photon reconstruction

figure 4.4a shows the reduction in fragments identified as photons, using a single photon per event sample, comparing photon reconstructions. The number of photon stays below 1.05, where the true value is 1, even at high energy. A similar trends shows in figure **??**, where the extra fragments identified as neutral hadrons have taken into account.

figure 4.4a and figure **??**

The default histogram size is 41 by 41 bins.

The input of the two dimensional peak finding algorithm is a two dimensional histogram.
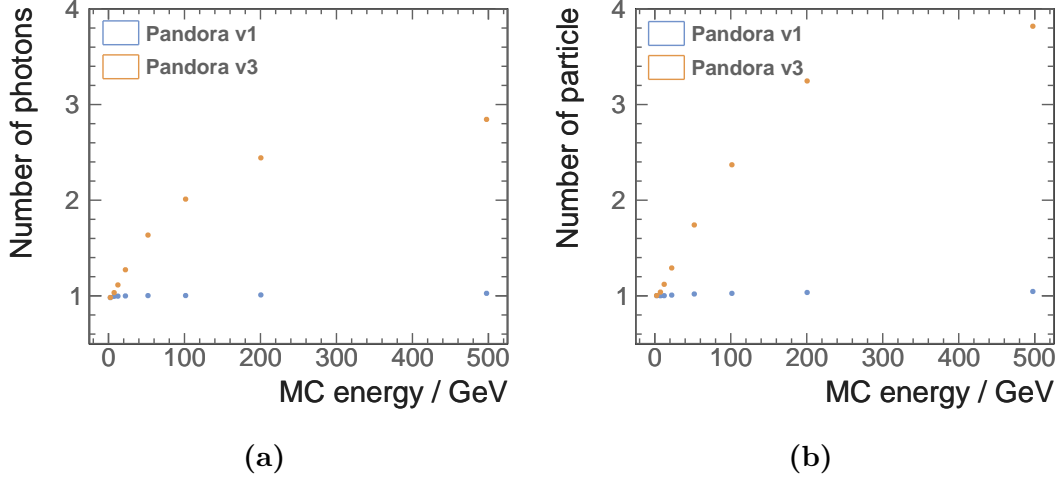
Figure 4.4: figure 4.4a and figure 4.4b shows the number of reconstructed photons and reconstructed particles, as a function of their true energy using a single photon per event sample. The top orange and bottom blue dots are reconstructed with PandoraPFA version 1 and version 3. The photon reconstruction is changed in PandoraPFA version 2.

Figure 4.5: figure 4.5a and figure 4.5b shows the number of reconstructed photons and reconstructed particles, as a function of the MC distance separation in the calorimeter, using a two photons per event sample. The top orange and bottom blue dots are reconstructed with PandoraPFA version 1 and version 3. The photon reconstruction is changed in PandoraPFA version 2.
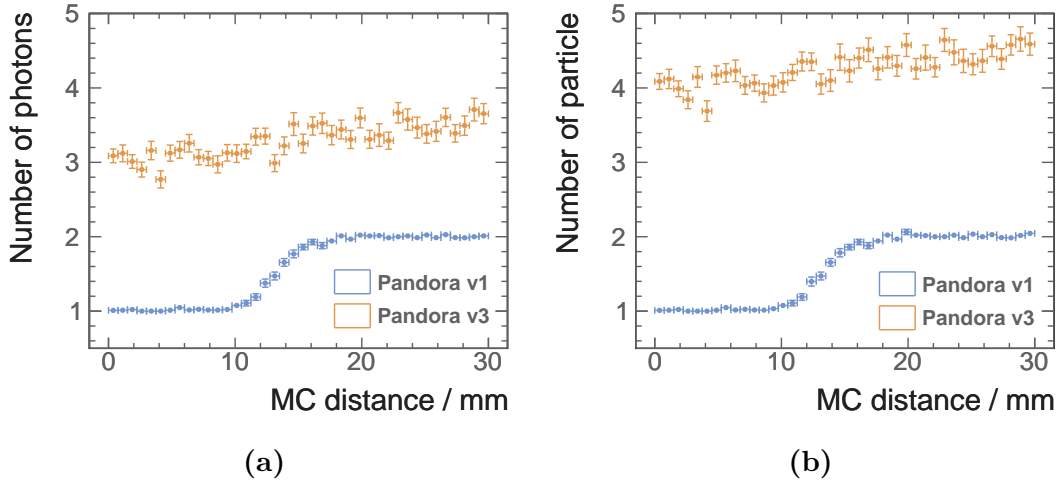
Chapter 5

Tau Lepton Final State Separation

"MVA: Turn numbers into gold."
    — TMVA

5.1 Introduction

Why study tau

Tau lepton has been examined closely in the past. The decay and the spin of the decay product were direct tests to the standard model. The spin of the decay product, using a Higgs decaying to tau tau channel, allows one to determine the spin of the higgs. Also, as tau is short-lived, only its decay products can be detected and reconstructed in the detector. Therefore, the ability to reconstruct and separate different tau decay modes is benchmark of detector performances.

This chapter will describe a tau final decay separation study. The processor developed for the study is used to test different detector models, as a proof-of-principle of detector optimisation using tau decay separation. Lastly, the spin of the Z was studied using one Z decaying to two tau tau channel.

5.2 Simulation and reconstruction

$e^-e^+ \to \tau^-\tau^+$ channel is used for the tau decay mode separation study. Generator software WHIZARD 1.95 [3] is used to generated simulated Monte Carlo (MC) samples. Hadronisation is described with PYTHIA 6.4 [4], which is tuned to the LEP results []. The spin effect of tau lepton decay is described by TAUOLA [5].

Final state radiation (FSR) was simulated. The initial state radiation (ISR) and the beam induced background were not simulated.

Events were simulated with the CLIC_ILD detector concept, using software with MOKKA [6], based on the GEANT 4 package [7]. Events were reconstructed with ilcsoft version v01-17-07 [8] and PandoraPFA version v02-02-00 [9], where the photon reconstruction is described in [10].

5.3 Generator level cut

To study the difference between different tau decay modes, clear topological difference is required. Therefore, events was considered if the event passes a set of cuts at generator level, listed here

- the final state photons not converting to electron pair in the tracker,

- the tau leptons decaying in the barrel and the end cap regions, which are defined as polar angle between 0.3 to 0.6 rad and 0.8 to 1.57 rad, and

- the visible energy of the tau lepton decay products more than 5 GeV, where the visible energy of the tau lepton decay is defined as the energy of the tau minus the energy of the tau neutrino.

The angular requirement is due to the gap region between the barrel and and the end cap of calorimeters, which degrades the PFO resolution significantly.

Around two million events were simulated for this study.

Table 5.1: Branching ratios of the seven major τ^- decays, taken from [11]. τ^+ decays similarly to τ^-.

Decay final state	Branching ratio / %
$e^- \, \overline{\nu}_e \, \nu_\tau$	17.83 ± 0.04
$\mu^- \, \overline{\nu}_\mu \, \nu_\tau$	17.41 ± 0.04
$\pi^- \, \nu_\tau$	10.83 ± 0.06
$\rho(\pi^-\pi^0)_{770}\nu_\tau$	25.52 ± 0.09
$a_1(\pi^-\pi^0\pi^0)_{1260}\nu_\tau$	9.30 ± 0.11
$a_1(\pi^-\pi^-\pi^+)_{1260}\nu_\tau$	8.99 ± 0.06
$\pi^- \, \pi^- \, \pi^+ \, \pi^0 \, \nu_\tau$	2.70 ± 0.08

5.4 Decay modes

Seven major decay final states of the tau lepton shown in table 5.1 were studied, covering $92.58\,\%$ of all tau decays [11]. Decay modes not listed in the table have branching fractions lower than 1% each. These final states can be classified into three categories: leptonic decays ($e^- \, \overline{\nu}_e \, \nu_\tau$ and $\mu^- \, \overline{\nu}_\mu \, \nu_\tau$), one-prong with photons ($\pi^- \, \nu_\tau$, $\rho(\pi^-\pi^0)_{770}\nu_\tau$ and $a_1(\pi^-\pi^0\pi^0)_{1260}\nu_\tau$), and three-prong with photons ($a_1(\pi^-\pi^-\pi^+)_{1260}\nu_\tau$ and $\pi^- \, \pi^- \, \pi^+ \, \pi^0 \, \nu_\tau$).

The studied channel, $e^-e^+ \to \tau^-\tau^+$, contains two τ decaying in opposite directions. To select decay products of one τ, the fiducial detector space was divided into two halves. Event shape variable thrust is used to separate two halves. The classical event shape thrust [**?**], is defined as

$$T = \max_{\hat{t}} \frac{\sum_i \left| \hat{t}{\cdot}\vec{p_i} \right|}{\sum_i |\vec{p_i}|} \tag{5.1}$$

where $\vec{p_i}$ is the momentum vector of the particle i. Summation is over all particles in the event. Thrust axis, $\hat{t}$, is a unit vector. (Principle) Thrust value, T, is 1 for a perfect pencillike back-to-back two-jet event, and 0.5 for a perfect spherical event. The sign of dot product between thrust axis and PFO momentum determines which half the PFO falls into.
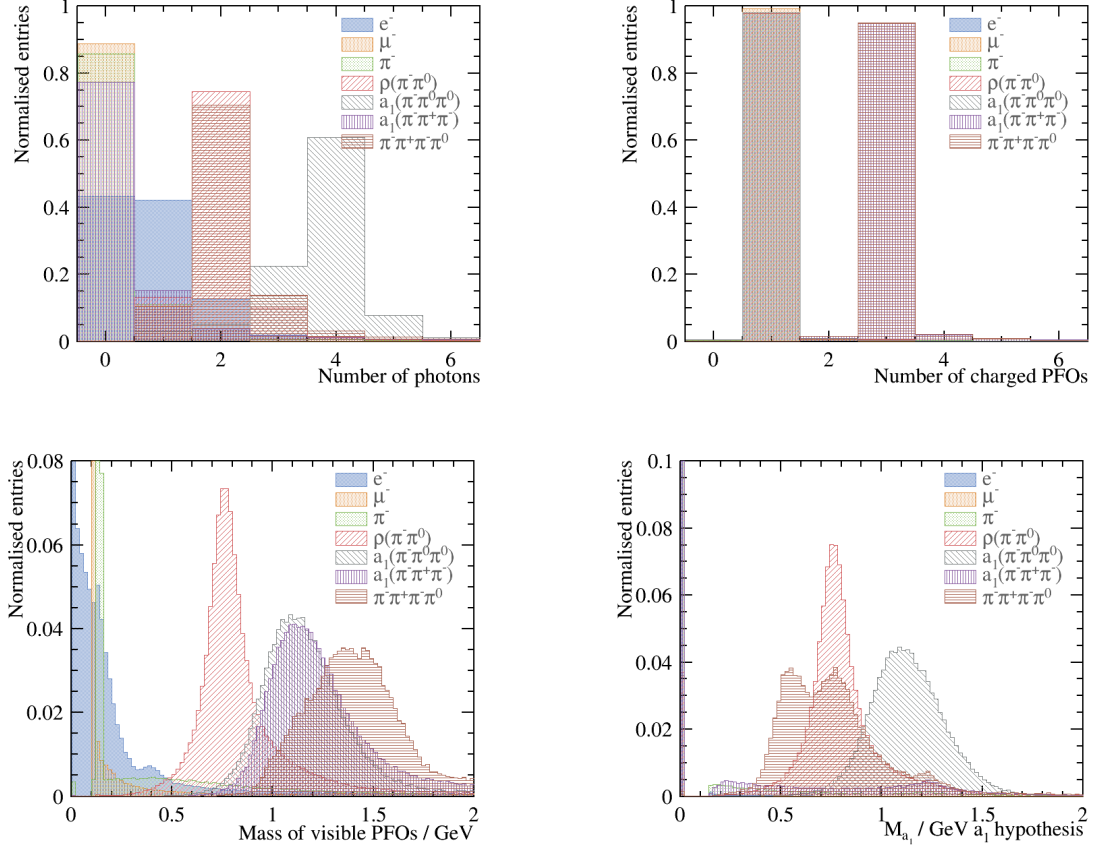
5.5 Discriminative variables

Figure 5.1: Normalised distribution for selected discriminative variables for seven final states, $e^- \, \bar{\nu}_e \, \nu_\tau$, $\mu^- \, \bar{\nu}_\mu \, \nu_\tau$, $\pi^- \, \nu_\tau$, $\rho(\pi^- \pi^0)_{770} \nu_\tau$, $a_1(\pi^- \pi^0 \pi^0)_{1260} \nu_\tau$, $a_1(\pi^- \pi^- \pi^+)_{1260} \nu_\tau$ and $\pi^- \, \pi^- \, \pi^+ \, \pi^0 \, \nu_\tau$, separated using truth information, for $\sqrt{s} = 100 \, \text{GeV}$ for nominal CLIC_ILD detector model. The top left, top right, bottom left and bottom right plots are the normalised entries against the number of photons, number of charged PFOs, invariant mass of visible PFOs, and the invariant mass of $a_1(\pi^- \pi^0 \pi^0)_{1260}$ for hypothesis test, respectively. There is a clear distinction between different final states in each plot.

Some variables with most discriminative power are shown in figure **??**. In total 29 variables used in the multivariate analysis. The reason for the large number of variables is due to training seven decay modes at once, which will be discussed later.

Here is a full list of all variables used in the multivariate analysis. Energy of the τ is assume to be the same as the energy of $e^\pm$ colliding beam, which is half of the $\sqrt{s}$ = e TeV nergy. Recoil momenta were calculated assuming the e^- e^+ collision happened

at the centre of mass energy. Both assumptions are largely valid when there is no ISR contribution.

- $\frac{E_{ECal,HCal}}{E_{tot}}$, charged: Sum of energy deposited in ECal and HCal, divided by the energy of charged particles

- $\frac{E_{ECal,HCal}}{E_{tot}}$, all: Sum of energy deposited in ECal and HCal, divided by the energy of all particles

- m_{vis}: Invariant mass of visible particles in GeV

- $\frac{E_{vis}}{E_{\tau^-}}$: Sum of energy of all particles, divided by the energy of τ^-

- $\frac{E_{charged}}{E_{\tau^-}}$: Sum of energy of charged particles, divided by the energy of τ^-

- $\frac{E_{\mu^-}}{E_{\tau^-}}$: Sum of energy of muons, divided by the energy of τ^-

- $\frac{E_{e^-}}{E_{\tau^-}}$: Sum of energy of electrons, divided by the energy of τ^-

- $\frac{E_{\gamma}}{E_{\tau^-}}$: Sum of energy of photons, divided by the energy of τ^-

- $\frac{E_{\pi^-}}{E_{\tau^-}}$: Sum of energy of charged pions, divided by the energy of τ^-

- $N_{charged}$: Number of charged particles

- N_{μ^-}: Number of muons

- N_{e^-}: Number of electrons

- N_{γ}: Number of photons

- N_{π^-}: Number of charged pions

- m_{γ}: Invariant mass of photons in GeV

- $m_{charged}$: Invariant mass of charged particles in GeV

- $m_{neutral}$: Invariant mass of neutral particles in GeV

- m_{π^-}: Invariant mass of charged pions in GeV

- $m_{\pi^0}, \rho(\pi^-\pi^0)_{770}$hypothesis: Fitted invariant mass of π^0 for $\rho(\pi^-\pi^0)_{770}$ hypothesis test

- $m_{\rho(\pi^-\pi^0)_{770}}$, $\rho(\pi^-\pi^0)_{770}$**hypothesis**: Fitted invariant mass of $\rho(\pi^-\pi^0)_{770}$ for $\rho(\pi^-\pi^0)_{770}$ hypothesis test

- $m_{\pi^0 1}$, $a_1(\pi^-\pi^0\pi^0)_{1260}$**hypothesis**: First fitted invariant mass of π^0, for $a_1(\pi^-\pi^0\pi^0)_{1260}$ hypothesis test, ordered by closeness to the true π^0 mass

- $m_{\pi^0 2}$, $a_1(\pi^-\pi^0\pi^0)_{1260}$**hypothesis**: Second fitted invariant mass of π^0, for $a_1(\pi^-\pi^0\pi^0)_{1260}$ hypothesis test, ordered by closeness to the true π^0 mass

- $m_{a_1(\pi^-\pi^0\pi^0)_{1260}}$, $a_1(\pi^-\pi^0\pi^0)_{1260}$**hypothesis**: Second fitted invariant mass of $a_1(\pi^-\pi^0\pi^0)_{1260}$, for $a_1(\pi^-\pi^0\pi^0)_{1260}$ hypothesis test

- $\overline{E}_{cell}$: Average energy deposited in a calorimeter cell in GeV

- $d_{trans,shower}$: Transverse shower width for electromagnetic shower profile, averaged for all clusters in the ECal

- $l_{long,shower}$: Longitudinal start layer for electromagnetic shower profile, averaged for all clusters in the ECal

- $\Delta l_{long,shower}$: Longitudinal discrepancy for electromagnetic shower profile, averaged for all clusters in the ECal

- $\%\text{MIP}$: Fraction of calorimeter hits registered as minimum ionised particles, averaged for all clusters in the ECal

- $\frac{E}{P}$: Energy divided by momentum, averaged for all clusters in the ECal

Number of photons is an important variable for separating decay modes. This information is only available due to the excellent photon reconstruction. Shown in figure **??**, the majority of $\mu^- \, \overline{\nu}_\mu \, \nu_\tau$, $\pi^- \, \nu_\tau$ and $a_1(\pi^-\pi^-\pi^+)_{1260}\nu_\tau$ final states have zero photon reconstructed. The $e^- \, \overline{\nu}_e \, \nu_\tau$ final state event have one photon reconstructed instead of zero, due to the FSR effect. $\rho(\pi^-\pi^0)_{770}\nu_\tau$ and $\pi^- \, \pi^- \, \pi^+ \, \pi^0 \, \nu_\tau$ have nearly 80% events with two reconstructed photons, whilst $a_1(\pi^-\pi^-\pi^+)_{1260}\nu_\tau$ have over 60% events with four reconstructed photons. The loss is efficiency is due to the increasing difficulty to separate nearby photons.

The number of charged PFOs can clearly separate the leptonic and 1-prong final states, from the 3-prong final states, shown in figure **??**. The efficiency of leptonic final states are over 98%.

The invariant mass of the visible PFOs shows clear differences between different final states. $\rho(\pi^-\pi^0)_{770}\nu_\tau$, $a_1(\pi^-\pi^0\pi^0)_{1260}\nu_\tau$ and $a_1(\pi^-\pi^-\pi^+)_{1260}\nu_\tau$ distribution show clear resonance at ρ and $a_1(1260)$. $e^- \bar{\nu}_e \nu_\tau$, $\mu^- \bar{\nu}_\mu \nu_\tau$ and $\pi^- \nu_\tau$ distribution show much smaller invariant mass and $\pi^- \pi^- \pi^+ \pi^0 \nu_\tau$ shows a large invariant mass than $a_1(1260)$. The $e^- \bar{\nu}_e \nu_\tau$ final state has a long tail of invariant mass due to the extra photons from the FSR.

$\frac{E_{ECal,HCal},charged}{E_{tot}}$ and $\frac{E_{ECal,HCal},all}{E_{tot}}$ are both very effective at picking out leptonic decay modes.

For final states containing ρ and $a_1(1260)$ resonance, it is useful to use minimisation test for right pairing of the resonance. We will use $a_1(\pi^-\pi^0\pi^0)_{1260}$ as an example. $\rho(\pi^-\pi^0)_{770}$ is very similar.

The minimisation of $a_1(\pi^-\pi^0\pi^0)_{1260}$ hypothesis states

$$\chi^2_{a_1(1260)} = \left(\frac{m_{a_1(1260),fit} - m_{a_1(1260)}}{\sigma_{a_1(1260)}}\right)^2 + \left(\frac{m_{\pi^0,fit} - m_{\pi^0}}{\sigma_{\pi^0}}\right)^2 + \left(\frac{m_{\pi^{0*},fit} - m_{\pi^0}}{\sigma_{\pi^0}}\right)^2 , \quad (5.2)$$

where $m_{\pi^0,fit}$ and $m_{\pi^{0*},fit}$ are the invariant masses of all possible two photons combinations, $\sigma_{a_1(1260)}$ and σ_{π^0} are the half width of the invariant mass distribution of reconstructed $a_1(1260)$ and π^0 using the truth information, and $m_{a_1(1260)}$ and m_π are the masses of $a_1(1260)$ and π^0, taken from [11]. If there are only two or three photons, the $\chi^2_{a_1(1260)}$ expression will be reduced and not including $m_{\pi^{0*},fit}$ term, assuming two photons are merged in the reconstruction. If there are fewer than two photons, the $\chi^2_{a_1(1260)}$ expression would only contain $m_{a_1(1260),fit}$ term.

For the $\rho(\pi^-\pi^0)_{770}\nu_\tau$ final state, a similar $\chi^2_{\rho(770)}$ test for $\rho(770)$ hypothesis is used to extract $m_{\rho(770),fit}$ and $m_{\pi^0,fit}$ variables. $\chi^2_{\rho(770)}$ is similar to $\chi^2_{a_1(1260)}$ with $\rho(770)$ replacing $a_1(1260)$ and only one $m_{\pi^0,fit}$ term.

figure **??** shows the $m_{a_1(1260),fit}$ where $\rho(\pi^-\pi^0)_{770}\nu_\tau$, $a_1(\pi^-\pi^0\pi^0)_{1260}\nu_\tau$ and $\pi^- \pi^- \pi^+ \pi^0$ ν_τ final states contribute to the $a_1(1260)$ resonance, although only $a_1(\pi^-\pi^0\pi^0)_{1260}\nu_\tau$ final has a real $a_1(1260)$ resonance. This is due to the structure of the $\chi^2_{a_1(1260)}$ minimisation function allowing final states with more than two photons and one $\pi^\pm$ to contribute.

Last six variables in the list help to differentiate an electron final state to that of a charged pion. A charged pion that starts showering early in the calorimeter could have a

similar topology to an electromagnetic shower. Nevertheless, a good separation between the two can be achieved with the help of these variables.

5.6 Multivariate Analysis

For the multivariate analysis, the multiclass class of the TMVA package [?] was used to perform a multiclass classification, which trains the seven final states simultaneously. The multiclass class is an extension of the standard two-class signal-background classifier.

There are two ways for the training. "One v.s. one" is each class is trained against each other class. And the overall likelihood is normalised. The second way to train is called "one v.s. all", which is when each class is trained against all other classes.

Using a three-class example, A, B and C, "one v.s. one" scheme trains A against B, B against C, and C against A. Then the likelihood is normalised. "One v.s. all" would train A against B plus C, B against A plus C, and C against A plus B.

TMVA multiclass implementation uses "one v.s. all" scheme. For each final state, the multiclass classifier will train the final state as the signal against all other final states as the background. This process is repeated for each final state. The classifier output for a single event is a normalised response for each final state, where the sum is one. The response of each final state of a event can be treated as the likelihood. The event is classified into a particular final state if the final state has the highest classifier output response. The advantage of using the multiclass is that the correlation between different final states are accounted for and the classifier output are correctly adjusted for multiple final states, hence one event can only be classified into one final state. The issue with the multiclass is that discriminative variables for each final state need enter the training stage, resulting in a large number of variables.

Half of the randomly selected samples were used in the training process and the other half were used for testing.

The TMVA multiclass classifier used is boosted decision tree with gradient boosting (BDTG), as it was found to give for the best performance. The MVA classifier is trained and optimised to give the best overall separation across all final states. MVA will be discuss further in section **??**

5.7 Result

Reco ↓ True →	$e^- \bar{\nu}_e$	$\mu^- \bar{\nu}_\mu$	π^-	$\rho(\pi^-\pi^0)$	$a_1(\pi^-\pi^0\pi^0)$	$a_1(\pi^-\pi^-\pi^+)$	$\pi^- \pi^- \pi^+ \pi^0$
$e^- \bar{\nu}_e$	**99.8**	-	0.9	1.1	0.8	-	-
$\mu^- \bar{\nu}_\mu$	-	**99.5**	0.5	-	-	-	-
π^-	-	0.3	**93.2**	0.9	-	0.4	-
$\rho(\pi^-\pi^0)$	-	-	4.1	**93.0**	10.5	0.6	2.8
$a_1(\pi^-\pi^0\pi^0)$	-	-	-	4.3	**88.2**	-	1.0
$a_1(\pi^-\pi^-\pi^+)$	-	-	1.0	0.3	-	**96.6**	6.9
$\pi^- \pi^- \pi^+ \pi^0$	-	-	-	0.4	0.4	2.4	**89.3**

Table 5.2: The percentage of reconstructed decay modes corresponds to underlying true decay modes, with $\sqrt{s} = 100\,\mathrm{GeV}$ for nominal CLIC_ILD detector model. Bold numbers show the correctly reconstructed percentages. Numbers less than 0.25% are not shown. Statistical uncertainties are less than 0.25%. Final states include ν_τ, which is not shown.

The reconstruction efficiencies for the seven final state of the tau decaying with c.o.m. energy of 100 GeV for the nominal CLIC_ILD detector are shown in table 5.2. The perfect reconstruction would result in only terms in the diagonal.

The unprecedented high classification rate has been achieved. The improvement of photon reconstruction described in section **??** improved the ability to separate 1-prong final state. Most notably, figure **??** shows number of photons have a high correct reconstruction efficiency.

For leptonic decay, the selection efficiency is above 99.5% as the tracking system have much better resolution than the calorimeter.

The $\mu^- \bar{\nu}_\mu$ final state has very clear topology, as muon deposits energy in the muon chamber. Therefore, there is little confusion with other final states.

$e^- \bar{\nu}_e$ final state is well separated, due to the specialised variables aimed to differentiate early hadronic shower to electromagnetic shower. However, there is still about 1% confusion in one prong final state.

For one prong final states, π^- , $\rho(\pi^-\pi^0)$, and $a_1(\pi^-\pi^0\pi^0)$, the confusion is mainly due to the imperfect separation of nearby photons, originated form π^0.

Similarly the confusion between 3-prong final state, $a_1(\pi^-\pi^-\pi^+)$, and $\pi^-\ \pi^-\ \pi^+\ \pi^0$ is caused by the inability to resolve photon pairs.

5.8 Electromagnetic calorimeter optimisaiton

As discussed above, the tau decay mode separation is an benchmark test of detector performance. The ability to resolve photon pairs is crucial to separate different 1-prong states, and different 3-prong state. One of the main feature of calorimeter design affecting the photon resolution is the size of electromagnetic calorimeter (ECal) cell for the high granular calorimeter. The finer ECal cell size is, the better resolution of reconstructing individual photons.

The classification is being tested with the impact of different $\sqrt{s}$ and different ECal square cell sizes. Around two million events were simulated at each $\sqrt{s} = 100,\ 200,\ 500$ and $1000\,\mathrm{GeV}$, with each different ECal square cell sizes of 3, 5, 7, 10, 15 and $20\,\mathrm{mm}$. Events were simulated and reconstructed in the same way as described above, with same selection applied. MVA classifier was trained individually for each $\sqrt{s}$ and each ECal square cell size, with same set of discriminative variables.

To access the impact different ECal square size on detector performance, in particular ECal performance, the correct reconstruction efficiency for 1-prong and 3-prong final states is used as metric. The higher $\sqrt{s}$ of the collision would degrade the performance, as photons are more boosted and more difficult to resolve.

The leptonic decay correct reconstruction efficiency is not used as a metric as they are similar across different ECal cell sizes. This is because the $e^{\pm}$ and $\mu^{\pm}$ identifications mostly rely on the tracking system, which was not varied in this study. The energy deposited in the calorimeter are used for the association to the tracks but it has a small impact on the lepton identification.

figure 5.2 shows that as the ECal cell sizes increase, the reconstruction efficiencies generally decrease. Larger cell sizes have lower spatial resolutions, making the separating of nearby photons more difficult.

For the $a_1(\pi^-\pi^0\pi^0)_{1260}\nu_\tau$ final state, the selection efficiency for $500\,\mathrm{GeV}$ rises from ECal cell sizes $15\,\mathrm{mm}$ to $20\,\mathrm{mm}$ and the one for $1000\,\mathrm{GeV}$ rises from 7 , to $20\,\mathrm{mm}$ actually goes up as cell size increases. This is because when the algorithm can not reconstruct
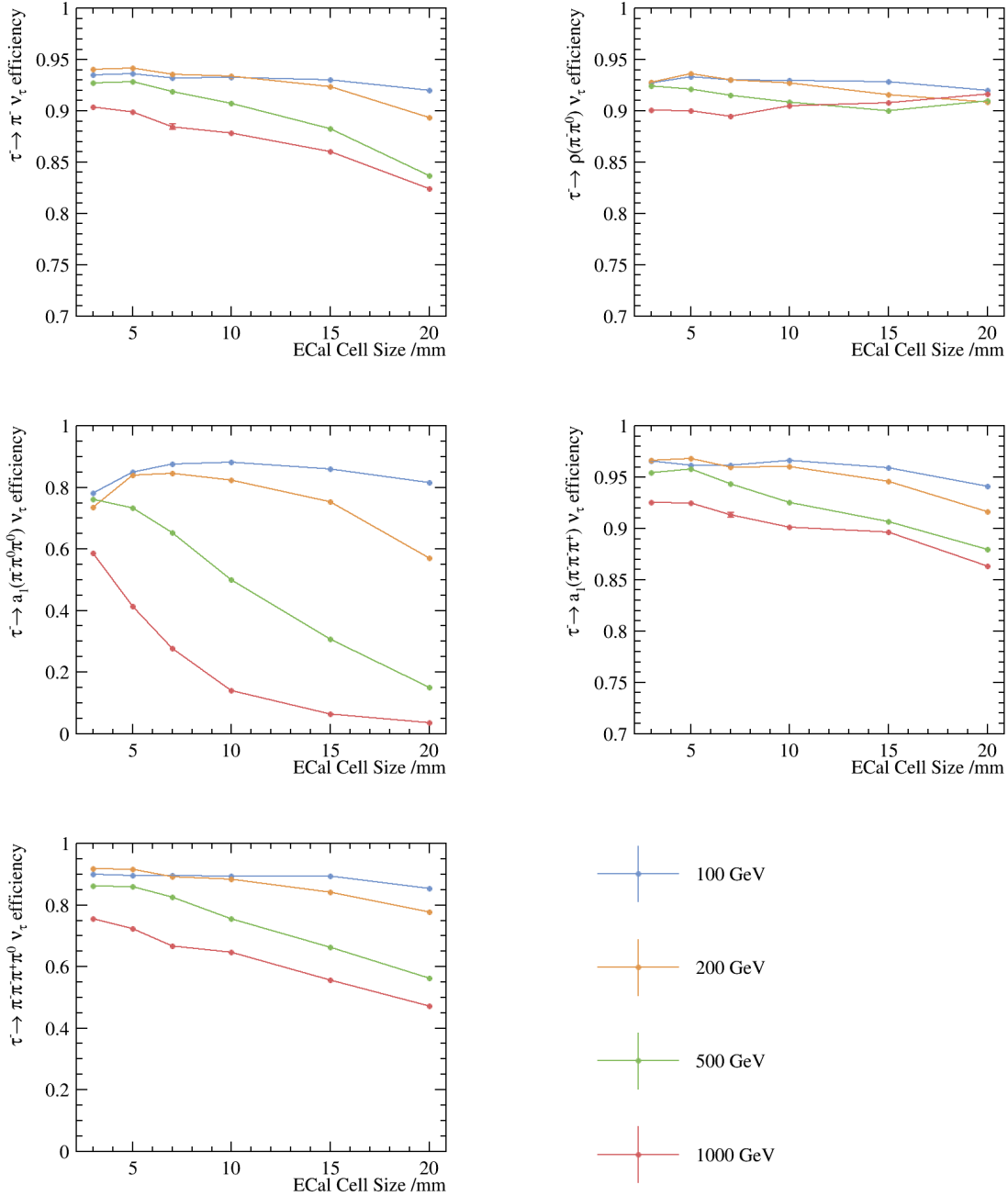
Figure 5.2: The selection efficiencies for various final states against the ECal cell size for different c.o.m. energies with the nominal CLIC_ILD detector model are shown. The top left, top right, middle left, middle right and bottom left plots are for the $\pi^- \, \nu_\tau$, $\rho\left(\pi^- \pi^0\right)_{770}\nu_\tau$, $a_1\left(\pi^- \pi^0 \pi^0\right)_{1260}\nu_\tau$, $a_1\left(\pi^- \pi^- \pi^+\right)_{1260}\nu_\tau$ and $\pi^- \, \pi^- \, \pi^+ \, \pi^0 \, \nu_\tau$ final states respectively. From the top to the bottom, blue, orange, green and red lines are representing the $\sqrt{s} = 100, 200, 500$ and $1000\,\mathrm{GeV}$ respectively.

four photons in the $a_1(\pi^-\pi^0\pi^0)_{1260}\nu_\tau$ final state, and the event topology would be very similar to the $\rho(\pi^-\pi^0)_{770}\nu_\tau$ final states.

For the $\sqrt{s} = = \text{TeV}\ 100$ and $200\,\text{GeV}$, the selection efficiency of the $5\,\text{mm}$ ECal cell size is better than that of the $3\,\text{mm}$. One possible explanation is that the and the PandoraPFA have been optimised for the nominal ILD detector with the $5\,\text{mm}$ ECal cell size, which shares the same ECal structure with the nominal CLIC_ILD detector.
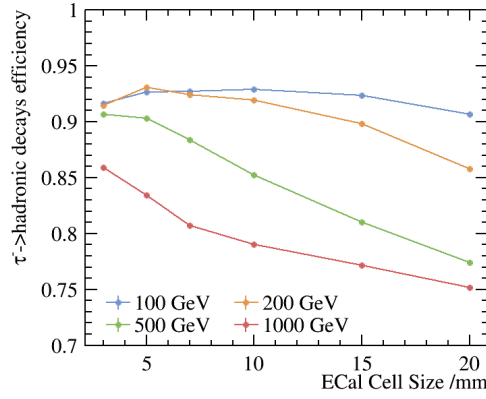
Figure 5.3: The τ hadronic decay efficiency against the ECal cell size for different $\sqrt{s} = $ e TeV nergies with the nominal CLIC_ILD detector model are shown. The blue, orange, green and red lines are representing the $\sqrt{s} = 100$, 200, 500 and $1000\,\text{GeV}$ respectively.

To effectively compare the overall separation power of all hadronic final states across $\sqrt{s}$ and ECal square cell sizes, we constructed a single parameter function, the τ hadronic decay final state efficiency function,

$$\varepsilon_{had} = \frac{\Sigma_i Br_i \varepsilon_i}{\Sigma_i Br_i}, \tag{5.3}$$

where Br_i is the branching fraction of a hadronic final state after the generator level cut. ε_i is the correct reconstruction efficiency of the final state, and the i is summing over five hadronic decay final state of τ. Leptonic decays, $e^-\,\overline{\nu}_e\,\nu_\tau$ and $\mu^-\,\overline{\nu}_\mu\,\nu_\tau$, were not included, because the variation of the leptonic decay selection efficiency is small.

In the figure 5.3, τ hadronic decay final state efficiency, ε_{had}, against the ECal cell size with different $\sqrt{s}$ is shown. ε_{had} decreases when cell sizes increases and when $\sqrt{s}$ increases. ε_{had} of the $5\,\text{mm}$ ECal cell size is better than that of the $3\,\text{mm}$ for $\sqrt{s} = 100$

and 200 GeV lines possibly due the optimisation of the software for the nominal ILD 5 mm ECal square cell size.

The ε_{had} is above 90% for the ECal cell size from 3 to 20 mm for the $\sqrt{s} = 100$ GeV. For $\sqrt{s} = 200$ GeV, the ε_{had} decreases from over 90% to 86% for the ECal square cell size from 3 to 20 mm. The degradation of the ε_{had} is more significant for the $\sqrt{s} = 500$ and 1000 GeV, where the ε_{had} drops from over 90% to 77% and from 86% to 75% respectively, over the same range of ECal square cell size.

For $\sqrt{s} = 100$ and 200 GeV, up to 15 mm cell sizes of ECal will give a good performance for τ hadronic decay modes separation, and the ε_{had} is above 90%. For $\sqrt{s} = 500$ and 1000 GeV, it is preferential to have a small ECal cell size for a good τ hadronic decay modes separation. There is about 15% degradation of ε_{had} for ECal square cell size from 3 to 20 mm.

5.9

Chapter 6

Double Higgs Bosons Production Analysis

"Two is better than one"
    — Sir Steve Orange, 1785–1854

6.1 Analysis Straggly Overview

Proof-of-principle study was perform at CLIC using CLIC_ILD detector model for $\sqrt{s} = 1.4\,\text{TeV}$ and $3\,\text{TeV}$. Simulated samples, including those containing double higgs production were used. Signal events, events with double higgs production, were selected via a set of carefully designed and complicated methods. g_{HHH} and g_{WWHH} are extracted simultaneously with template fitting with modified couplings samples.

6.2 Monte Carlo Sample Generation

Single channel is defined as $e^-e^+ \to HH\nu\overline{\nu}$. It is divided into sub-channel $HH \to b\overline{b}W^+W^-$ and $HH \to b\overline{b}b\overline{b}$ to allow closer examination and an improvement of signal selection when combined. In particular, I studied $HH \to b\overline{b}W^+W^-$ sub-channel.

    Selected background samples, including processes initiated by photons, are considered in the analysis and listed in Table **??**. These background were expected share similar

topologies with the signal process. When describing a multi-quark final state, it is referring to all final states of the same number of quarks, including final states with possible additional neutrinos and or leptons. A multi-quark final state does not include higgs production, unless explicitly stated.

Two-quark and four-quark final states were considered. Since the significant presence of beamstrahlung, where photon produced due to the high electric field generated by the colliding beams, processes initiated by photons are also included.

Processes invloving real photons from beamstrahlung (BS) and "quasi-real" photons are generated separately. For the "quasi-real" photon initiated processes, the Equivalent Photon Appproximation (EPA) has been used.

Photon-electron/photon-photon interactions with four-quark final states were considered. Photon-electron interaction with two-quark final state, one Higgs, and one neutrino is considered. Photon-electron interaction with two-quark final state, one Higgs, and one lepton is not considered due to its negligible cross section.

Single higgs productions are not considered because topologies are very different to the single process. Six-quark final states were not considered due to computational limitation.

For processes involving Higgs production explicitly, simulated Higgs mass is 126 GeV. As multi-quark final state background samples could, in principle, contain double higgs production, they are generated with a Higgs mass of 14 TeV. This will produce negligible double higgs production cross section.

All samples are generated with WHIZARD 1.95 [], taking into account the expected CLIC luminosity spectrum. PYTHIA 6.4 [] tuned on LEP data [] is used to describe fragmentation, hadronisation processes, and Higgs decays. TAUOLA [] is used for τ lepton decays.

Simulation

For most background processes, events are simulated when invariant mass of quarks are above 50 GeV. For electron-photon interaction with four quarks and a neutrino final state, events are simulated when invariant mass of quarks are above 120 GeV. These limits are necessary to generate a large amount of background samples in a feasible time, without losing much signal samples.

Finally, the main beam induced background $\gamma\gamma \to$ `hadrons` is simulated and overlayed [] to all samples according to the integration time of each subdetector.

6.3 Physics object and event reconstruction

Simulation is performed by MOKKA, interfacing GEANT 4. The reconstruction is done via Marlin in iLCSoft v01-16. Separate software package (processor) exists for identification of electrons, muons, taus, and jet reconstruction. New processors have been developed and existing processors have been optimised for a compromise of signal selection and background rejection. The latest function flavour tagging processor exist in iLCSoft v01-16, which prevented the usage of more recent iLCSoft.

For my signal channel, $HH \to b\bar{b}W^+W^-$, there is no lepton in the final state. Hence a effective lepton identifier would improve the signal identification. Processors are wither developed or optimised with samples at $\sqrt{s} = 1.4\,\text{TeV}$, and checked against samples at $\sqrt{s} = 3\,\text{TeV}$. Because the expected signal significance would be low, the processors are optimised to reject more background at the cost of losing a bit more signals, to increase the signal significance. It was found that the same set of parameters work well under $\sqrt{s} = 1.4\,\text{TeV}$ and $3\,\text{TeV}$.

6.3.1 Electron and muon identification

IsolatedLeptonFinderProcessor

In Marlin package, IsolatedLeptonFinderProcessor has been used. The optimal parameters ware chosen in collaboration and tested. The particle is identified as an isolated light lepton if it passes a chain of cuts.

A charge track is considered if it has more than $15\,\text{GeV}$ energy. An electron is identified if the energy in the ECal is over 90% of the total calorimetric energy. A muon is identified if the energy in the ECal is between 5% and 25% of the total calorimetric energy. Furthermore, only primary track is selected, which requires the Euclidean distance in the x-y plane, the in z direction, and in the x-y-z three dimensional space of the track starting point to the impact point to be less than $0.02\,\text{mm}$, 0.03mm, and $0.04\,\text{mm}$, respectively.

Channel	$\sigma(\sqrt{s} = 1.4\,\mathrm{TeV})$ / fb	$\sigma(\sqrt{s} = 3\,\mathrm{TeV})$ / fb
$e^- e^+ \to HH\nu\overline{\nu}$	0.149	0.588
$e^- e^+ \to q_l q_l H\nu\overline{\nu}$	0.86	1.78
$e^- e^+ \to c\overline{c}H\nu\overline{\nu}$	0.36	1.12
$e^- e^+ \to b\overline{b}H\nu\overline{\nu}$	0.31	1.91
$e^- e^+ \to qqqq$	1245.1	546.5*
$e^- e^+ \to qqqq\ell\ell$	62.1*	169.3*
$e^- e^+ \to qqqq\ell\nu$	110.4*	106.6*
$e^- e^+ \to qqqq\nu\overline{\nu}$	23.2*	71.5*
$e^- e^+ \to qq$	4009.5	2948.9
$e^- e^+ \to qq\ell\nu$	4309.7	5561.1
$e^- e^+ \to qq\ell\ell$	2725.8	3319.6
$e^- e^+ \to qq\nu\nu$	787.7	1317.5
$e^- \gamma(\mathrm{BS}) \to e^- qqqq$	1160.7	1268.7*
$e^+ \gamma(\mathrm{BS}) \to e^+ qqqq$	1156.3	1267.6*
$e^- \gamma(\mathrm{EPA}) \to e^- qqqq$	287.1	287.9*
$e^+ \gamma(\mathrm{EPA}) \to e^+ qqqq$	286.9	287.8*
$e^- \gamma(\mathrm{BS}) \to \nu qqqq$	79.8†	262.5*
$e^+ \gamma(\mathrm{BS}) \to \overline{\nu} qqqq$	79.3†	262.3*
$e^- \gamma(\mathrm{EPA}) \to \nu qqqq$	17.4†	54.2*
$e^+ \gamma(\mathrm{EPA}) \to \overline{\nu} qqqq$	17.3†	54.2*
$e^- \gamma(\mathrm{BS}) \to qqH\nu$	15.8*	58.6*
$e^+ \gamma(\mathrm{BS}) \to qqH\nu$	15.7*	58.5*
$e^- \gamma(\mathrm{EPA}) \to qqH\nu$	3.39*	11.7*
$e^+ \gamma(\mathrm{EPA}) \to qqH\nu$	3.39*	11.7*
$\gamma(\mathrm{BS})\gamma(\mathrm{BS}) \to qqqq$	21406.2*	13050.3*
$\gamma(\mathrm{BS})\gamma(\mathrm{EPA}) \to qqqq$	4018.7*	2420.6*
$\gamma(\mathrm{EPA})\gamma(\mathrm{BS}) \to qqqq$	4034.8*	2423.1*
$\gamma(\mathrm{EPA})\gamma(\mathrm{EPA}) \to qqqq$	753.0*	402.7*

Table 6.1: List of signal and background samples with the corresponding cross sections at $\sqrt{s} = 3\,\mathrm{TeV}$ and $\sqrt{s} = 1.4\,\mathrm{TeV}$. q can u, d, s, b or t. Unless specified, q, ℓ and ν represent particles and its corresponding anti-particles. γ (BS) represents a real photon from beamstrahlung (BS). γ (EPA) represents a "quasi-real" photon, simulated with the Equivalent Photon Approximation. For processes involving Higgs production explicitly, simulated Higgs mass is 126 GeV. Otherwise, Higgs mass is set to 14 TeV. For processes labeled with * and †, the generator level cut requires invariant mass of quarks greater than 50 and 120 GeV, respectively.

The isolation criteria states that

$$E_{cone}^2 \leqslant 5.7 \times E_l - 50 \tag{6.1}$$

where, E_{cone} is the total energy of PFOs within an opening angle of $\cos^{-1}(0.995)$ of the light lepton, and E_l is the energy of the light lepton.

BonoLeptonFinderProcessor

The IsolatedLeptonFinderProcessor is rather conservative. I developed a new more aggressive light lepton selection processor, BonoLeptonFinderProcessor, that utilises calorimetric information provided by PandoraPFA.

The processor uses two chains of cuts.

First chain uses the particle ID information from PandoraPFA. A electron is identified if it is a "PandoraPFA" electron and the energy in the ECal is over 95% of the total calorimetric energy. A muon is identified if it is a "PandoraPFA" muon. Primary track selection states the Euclidean distance in the x-y-z three dimensional space of the track starting point to the impact point to be less than $0.015\,\text{mm}$, and the PFO energy is more than $10\,\text{GeV}$. The light lepton either satisfy the high p_T requirement of at least $40\,\text{GeV}$, or the isolation criteria,

$$E_l \geqslant 23 \times \sqrt{E_{cone}} + 5 \tag{6.2}$$

where E_{cone} and E_l have the same definition as in the IsolatedLeptonFinderProcessor.

Second chain of cuts is similar to the IsolatedLeptonFinderProcessor. An electron is identified if the energy in the ECal is over 95% of the total calorimetric energy. A muon is identified if the energy in the ECal is between 5% and 20% of the total calorimetric energy. Primary track selection states the Euclidean distance in the x-y-z three dimensional space of the track starting point to the impact point to be less than $0.5\,\text{mm}$, and the PFO energy is more than $10\,\text{GeV}$. The light lepton either satisfy the high p_T requirement of at least $40\,\text{GeV}$, or the isolation criteria,

$$E_l \geqslant 28 \times \sqrt{E_{cone}} + 30 \tag{6.3}$$

where, E_{cone} is the total energy of PFOs within an opening angle of $\cos^{-1}(0.99)$ of the light lepton, and E_l is the energy of the light lepton.

Comparison: IsolatedLeptonFinderProcessor v.s. BonoLeptonFinderProcessor

Two processors share similar criterion for light lepton identification. The main difference is that the BonoLeptonFinderProcessor allows high p_T light lepton to be identified in a potential non-isolated environment, which leads to the more aggressiveness of the BonoLeptonFinderProcessor. The performance of two processors on the signal and selected background samples is shown in table 6.2

6.3.2 Tau identification

TauFinderProcessor

With a decay length of $87\mu m$, tau leptons decay before reaching the detector and can only be identified through the reconstruction of their decay products. The leptonic decay of tau can be identified using the two isolated lepton finder processor. Therefore tau identification will focus on the hadronic decay.

TauFinderProcessor [12], an existing processor Marlin package, has been tuned in collaboration and tested. The a collection of tau decay productions are identified they pass a chain of cuts.

Particles are not considered if p_T is less than $1\,\text{GeV}$ or $|\cos(\theta_z)|$ is more than $1.1\,\text{rad}$, as they are more likely from beam induced background. A seed is considered if a charged particle has p_T more than $10\,\text{GeV}$. A search cone of opening angle $0.03\,\text{rad}$ is then formed. The search cone is rejected if it has more than 3 charged particles, more than 10 particles or its invariant mass more than $2\,\text{GeV}$. An isolation cone is formed with opening angle between 0.03 and $0.33\,\text{rad}$ of the seed. The seed is rejected if there are more than $3\,\text{GeV}$ in the isolation cone.

BonoTauFinderProcessor

The TauFinderProcessor's performance is decent, but there is room for improvement. I developed a new more aggressive tau lepton selection processor, BonoTauFinderProcessor, that utilises calorimetric information provided by PandoraPFA.

Similar to the previous processor, PFOs with p_T less than $1\,\text{GeV}$ are rejected. A tau seed is defined as a charged particle with p_T at least $5\,\text{GeV}$. The search cone has an opening angle of $\cos^{-1}(0.999)$. Particles are iteratively added to the search cone according to the size of the opening angle to the seed. A temporary search cone is then considered if it has one or three charged particles, and the invariant mass is less than $3\,\text{GeV}$. The search cone needs to satisfy one of isolation criterion.

1. No particle in the large isolation cone, and p_T of search cone at least $10\,\text{GeV}$,

2. One charged particle in the search cone, one particle in the large isolation cone, and r_0 larger than $0.01\,\text{mm}$,

3. Three charged particle in the search cone, one particle in the large isolation cone, p_T of search cone at least $10\,\text{GeV}$, and search cone opening angle less than $\cos^{-1}(0.9995)$,

4. One charged particle in the search cone, no particle in the small isolation cone, r_0 larger than $0.01\,\text{mm}$, and p_T of search cone at least $10\,\text{GeV}$,

5. Three charged particle in the search cone, no particle in the small isolation cone, p_T of search cone at least $10\,\text{GeV}$, and search cone opening angle less than $\cos^{-1}(0.9995)$,

where large and small isolation cone are defined as opening angle of $\cos^{-1}(0.95)$, and $\cos^{-1}(0.99)$ respectively. If there are multiple temporary search cone of a same seed passing the isolation criteria, the cone with smallest opening angle is chosen for output.

Comparison: TauFinderProcessor v.s. BonoTauFinderProcessor

Two processors share similar size of search cone and isolation cone. The BonoTauFinderProcessor has looser cut on minimum p_T and invariant, but stricter isolation criterion. This leads to a more aggressive tau finder. The performance of two processors on the signal and selected background samples is shown in table 6.2

Selection / Efficiency (1.4 TeV)	Signal	$qqqq\ell\nu$
IsolatedLeptonFinderProcessor	99.3%	50.3%
BonoLeptonFinderProcessor	99.1%	39.9%
TauFinderProcessor	97.5%	52.3%
BonoTauFinderProcessor	89.7%	38.5%
ForwardFinderProcessor	98.9%	95.1%
Combined	86.6%	16.8%
Processor / Efficiency (3 TeV)	Signal	$qqqq\ell\nu$
IsolatedLeptonFinderProcessor	99.5%	66.8%
BonoLeptonFinderProcessor	99.0%	52.5%
TauFinderProcessor	97.7%	79.5%
BonoTauFinderProcessor	86.3%	60.3%
ForwardFinderProcessor	95.9%	80.7%
Combined	81.0%	23.3%

Table 6.2: isolated lepton finder processors performance on the signal and selected background samples.

6.3.3 Very forward electron identification

Certain background channels, for example photon-electron interactions, contain electrons in the very forward part of the detector, namely LCal and BCal. These forward calorimeters were not simulated due to computational limitation. Most particle in these detector would be very forward particles from beam induced background. However, previous study has shown [] that high energy electrons can be identified with high efficiency. Due to the lack of tracking in these region, electrons and photons would have the same electromagnetic shower profile, with the given calorimeter resolution. MC photons and electrons are checked if they fall in the LCal or the BCal, and checked against the known detection efficiency.

Beam Calorimeter acceptance is defined as $|\cos(\theta_Z)|$ is between 0.01 and 0.04 rad and length in z direction is between 3181 and 3441 mm. Luminosity Calorimeter acceptance is defined as $|\cos(\theta_Z)|$ is between 0.038 and 0.11 rad and length in z direction is between 2539 and 2714 mm. For $\sqrt{s} = (\text{TeV } 3)$, the BeamCal detection efficiency is provided by a software package []. For $\sqrt{s} = (\text{TeV } 1.4)$, the same software for the BeamCal is used, by scaling the energy of the MC particle by a factor of $\frac{3}{1.4}$. For the LumiCal, the

Selection / Efficiency (1.4 TeV)	Signal	$e^-\gamma(BS) \rightarrow e^- qqqq$
Combined light lepton finder	87.6%	67.5%
ForwardFinderProcessor	98.9%	53.6%
Combined	86.6%	30.8%
Processor / Efficiency (3 TeV)	Signal	$e^-\gamma(BS) \rightarrow e^- qqqq$
Combined light lepton finder	84.4%	72.7%
ForwardFinderProcessor	95.9%	55.4%
Combined	81.0%	33.4%

Table 6.3: Very forward electron and photon finder performance on the signal and selected background samples.

identification efficiency is defined as

$$
\varepsilon = \begin{cases} 0, & \text{if } E < 50\,\text{GeV} \\ 0.99 \times \frac{(\text{erf}(E-100)+1)}{2}, & \text{otherwise} \end{cases} \tag{6.4}
$$

where E is the energy of the electron or the photon.

The background rejection is significant, shown in table **??** for the signal and selected background.

6.3.4 Other lepton identification processors

Other isolated lepton selection processors available in Marlin package, including IsolatedLeptonTagging and TauJetClustering, have been tested. The results, after some tuning of parameters, were unsatisfactory. They either performed poorly comparing to the processors above, or became redundant after the processors above. Therefore, these processors were not used in this analysis.

6.4 Jet reconstruction

The signal channel, $HH \rightarrow b\bar{b}W^+W^- \rightarrow b\bar{b}qqqq$, is a four-jet final state. A useful technique for the analysis is to reconstruct the four-jet final state using jet algorithms. This allows discriminative variables to be calculated.

6.4.1 Jet reconstruction optimisation

Longitudinal invariant, k_t, jet algorithm was chosen for the jet clustering. Due to the presence high level of beam induced background at the CLIC, it has been shown that a jet algorithm designed for hadron colliders are more effective than those traditional designed for the electron-positron collider, such as Durham algorithm. []

The free parameters for k_t algorithm is the R parameter, which controls the fatness of the jet. There is also the choice of the PFO collection, which incorporate different level of time and p_T cuts, to reduce beam induce background. Both parameters are optimised for $\sqrt{s} = 1.4\,\text{TeV}$ and $\sqrt{s} = 3\,\text{TeV}$.

The details of jet algorithm can be found in section **??**.

The R parameter of the k_t jet algorithm, and the collection of the PFOs are chosen to give the best invariant mass resolution. When there are a few suitable candidate, analysis were performed in parallel. Decision were made to give the highest signal significance.

k_t jet algorithm was used as part of the FastJet algorithms available in the Marlin package.

The samples containing the signal, $HH \rightarrow b\bar{b}W^+W^- \rightarrow b\bar{b}qqqq$, was used for the optimisation of the jet reconstruction. The signal events were chosen using MC truth information.

Jet algorithm was run in exclusive mode, where number of jets is chosen to be six.

For the signal, $HH \rightarrow b\bar{b}W^+W^- \rightarrow b\bar{b}qqqq$, one Higgs decays to two b quarks, resulting in two jets from hadronisation. Similarly the other Higgs decays to two W bosons, where each W boson decays into two quarks. Therefore, the expected number of jets is six.

Jets produced by the k_t jet algorithm are paired up using MC truth information, to the corresponding Higgs and W boson. Four invariant mass distributions are obtained: two Higgs masses, $m_{H_{bb}}$, $m_{H_{WW^*}}$, and two W masses m_W, m_{W^*}. W^* indicates the off-mass-shell W boson, because when a Higgs decays into two W bosons, one W is off the mass shell, as the Higgs mass is less than the sum two W masses.

Three mass distributions are worth comparing for different jet reconstruction, namely, $m_{H_{bb}}$, $m_{H_{WW^*}}$, and m_W. The ideal jet reconstruction should produce the a sharp mass peak around the particle's true mass.
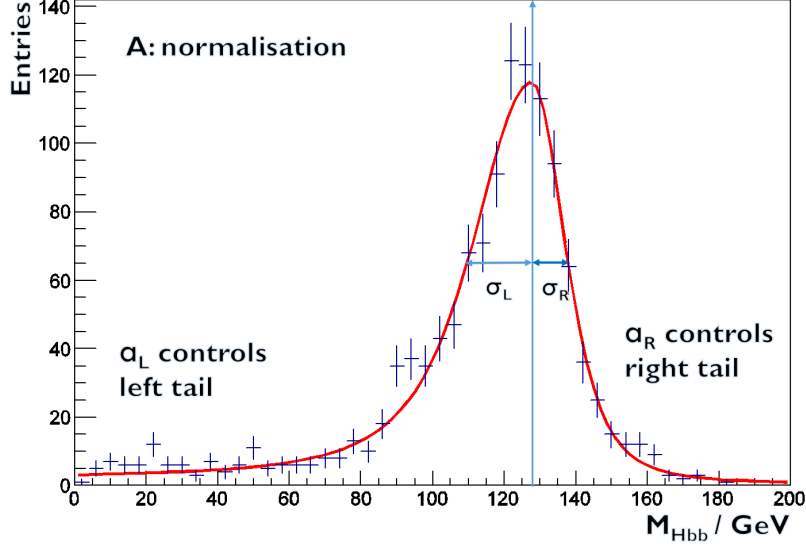
Figure 6.1: A typical example of MC mass fit of $m_{H_{bb}}$ for double higgs analysis. Red line indicates the best fit. Vertical arrow indicates the fitted peak position.

To quantitatively access the mass distribution, a gaussian like fit is performed to extract the position of the peak, and the width of the distribution. The fit has the form:

$$f(m) = A e^{-\frac{(m-\mu)^2}{g}} \begin{cases} g = 2\sigma_L + \alpha_L(m - \mu), & \text{if } m < \mu \\ g = 2\sigma_R + \alpha_R(m - \mu), & \text{if } m \geqslant \mu \end{cases} \tag{6.5}$$

The fit represents an asymmetrical gaussian function, where m is binned mass distribution, with 50 bins in range $[0, 200]$ GeV. The fitted mass peak is denoted by μ. σ_L and σ_R allow asymmetrical width of the distribution. α parameter controls the fit of tails. Inspired by the $t\bar{t}$ analysis [], the use of the α parameter allows the fit in the whole mass range, otherwise only the peak of the distribution should be fitted with a gaussian like function. A is the normalistion factor. An example of the fit of $m_{H_{bb}}$ is shown in figure 6.1.

For $\sqrt{s} = 1.4$ TeV, shown in figure 6.2, normal selected PFO with $R = 0.7$ give a good fitted mass for H_{WW^*} and W. The mass is slightly too low for the H_{bb}. figure **??** shows the combined relative fitted width for the H_{bb}, H_{WW^*} and W. Normal selected PFO with $R = 0.7$ gives an almost optimal relative width for H_{bb}, while achieving a good balance for H_{WW^*} and W. Therefore, normal selected PFO with $R = 0.7$ is chosen to be the optimal jet reconstruction parameters.
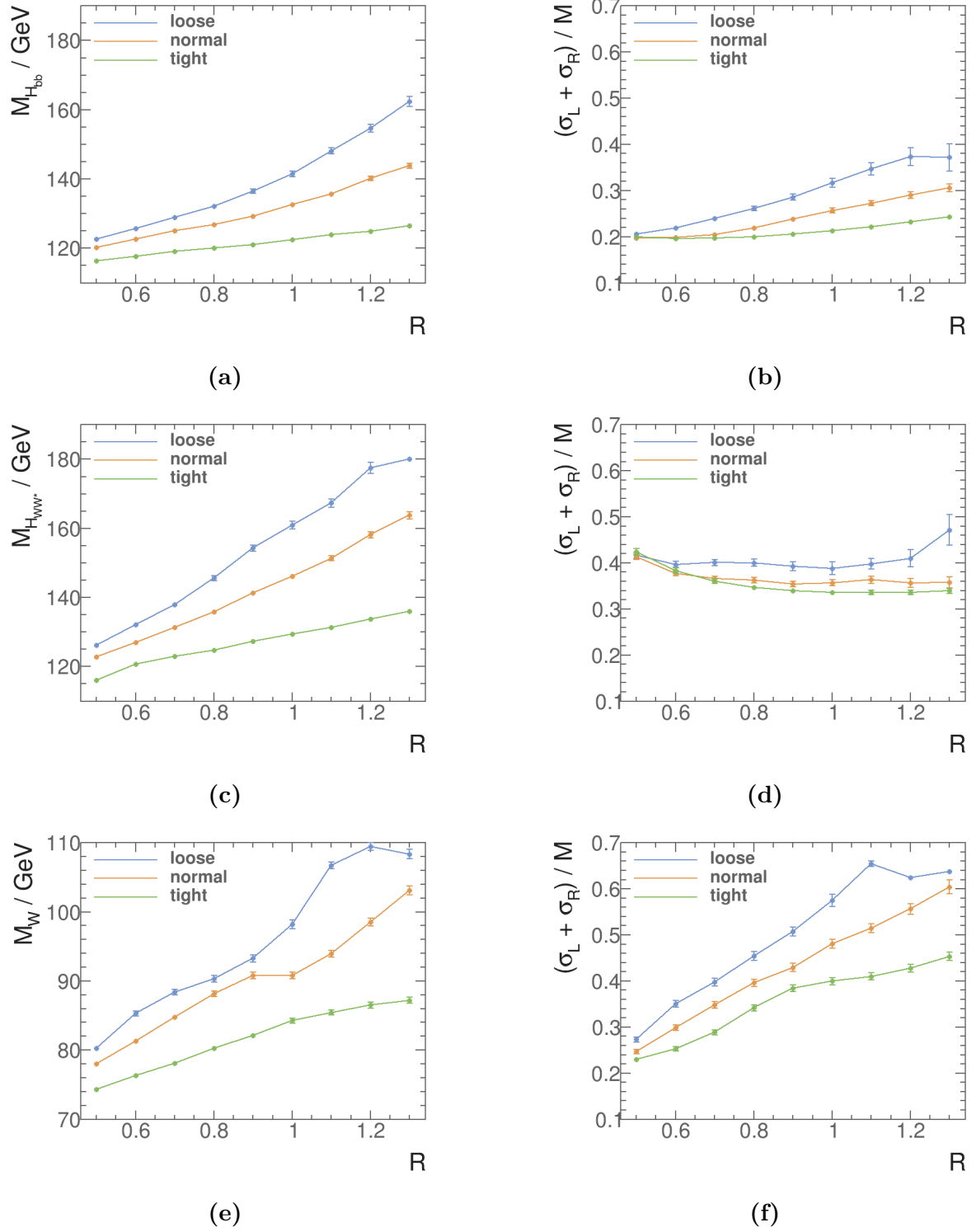
(a)

(b)

(c)

(d)

(e)

(f)
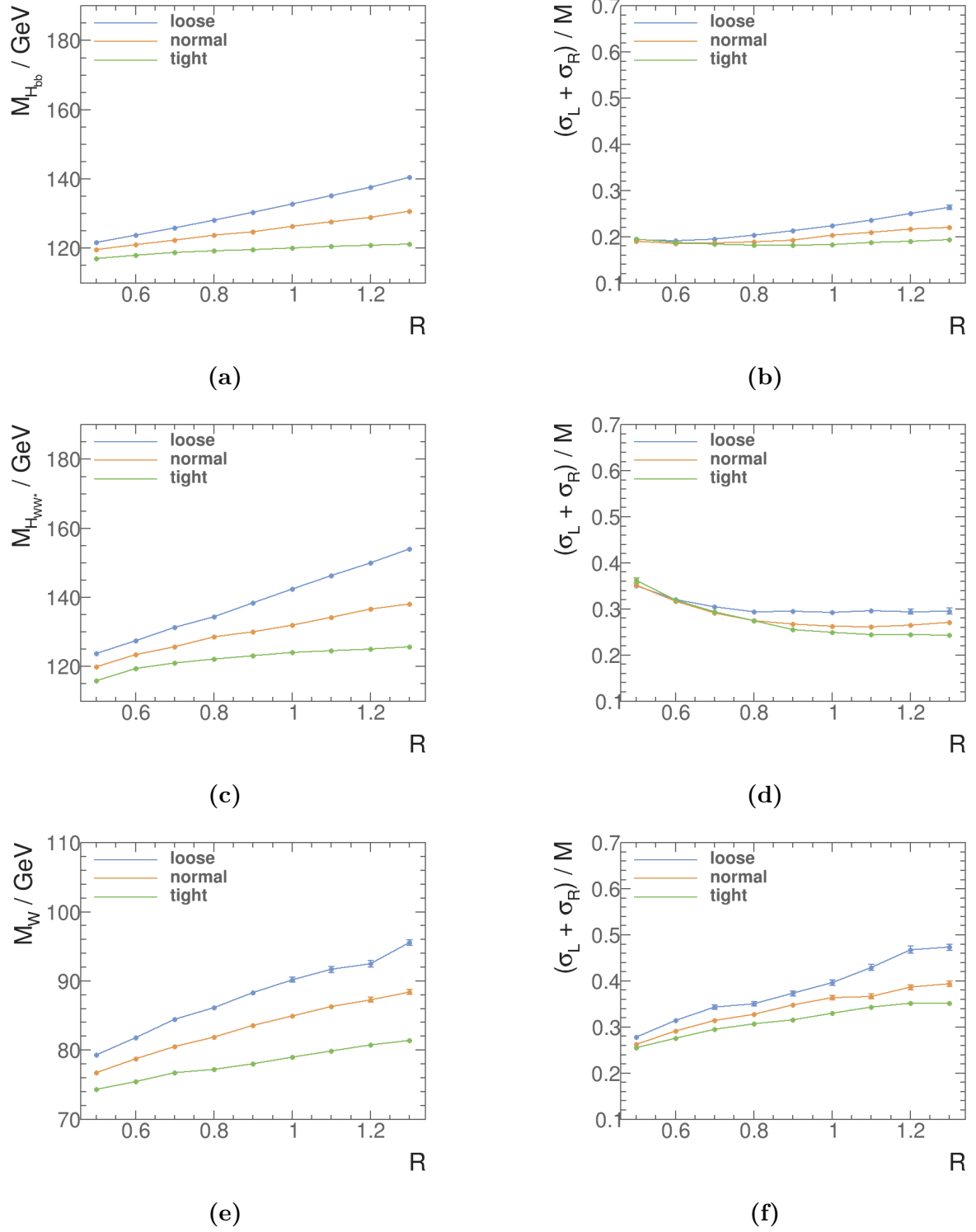
Figure 6.2: figure 6.2a, 6.2c, and 6.2e show fitted mass of H_{bb}, H_{WW^*}, and W, respectively, for loose, normal and tight selected PFO against R parameter, with $\sqrt{s} = 1.4\,\text{TeV}$. figure 6.2b, 6.2d, and 6.2f show fitted combined widths divided by the fitted masses of H_{bb}, H_{WW^*}, and W, respectively, for loose, normal and tight selected PFO against R parameter, with $\sqrt{s} = 1.4\,\text{TeV}$.

Jet Parameters	$\sqrt{s} = 1.4\,\text{TeV}$	$\sqrt{s} = 3\,\text{TeV}$
$\mu_{H_{bb}}$	$122.3_{\pm 0.2}$	$119.1_{\pm 0.3}$
$\sigma_{L,H_{bb}}$	$15.2_{\pm 0.2}$	$15.0_{\pm 0.3}$
$\sigma_{R,H_{bb}}$	$7.55_{\pm 0.16}$	$8.4_{\pm 0.2}$
$\mu_{H_{WW^*}}$	$125.7_{\pm 0.2}$	$123.0_{\pm 0.3}$
$\sigma_{L,H_{WW^*}}$	$29.4_{\pm 0.3}$	$36.6_{\pm 0.6}$
$\sigma_{R,H_{WW^*}}$	$7.18_{\pm 0.17}$	$7.4_{\pm 0.2}$
μ_W	$80.5_{\pm 0.2}$	$78.1_{\pm 0.3}$
$\sigma_{L,W}$	$16.2_{\pm 0.3}$	$13.1_{\pm 0.4}$
$\sigma_{R,W}$	$9.03_{\pm 0.16}$	$9.5_{\pm 0.2}$

Table 6.4: The extracted fitted parameters of optimal jet reconstructions, normal selected PFO with $R = 0.7$ for $\sqrt{s} = 1.4\,\text{TeV}$ and tight selected PFO with $R = 0.7$ for $\sqrt{s} = 3\,\text{TeV}$.

For $\sqrt{s} = 3\,\text{TeV}$, the choice is a bit more complicated. Shown in figure 6.3, fitted mass for H_{bb} favours normal selected PFO with $R = 0.8$. Fitted mass for H_{WW^*} favours tight selected PFO with $R = 0.9$. Fitted mass for W favours tight selected PFO with $R = 0.8$. Looking at the combined relative fitted width for the H_{bb}, H_{WW^*} and W, shown in figure **??**, normal selected PFO gives a larger width than tight selected PFO. Within tight selected PFO, small R values provide a shaper width for H_{WW^*} and H_{bb}, but a broader width for W. Therefore, tight selected PFO with $R = 0.7$ and $R = 1$ are both chosen for parallel analysis.

Later it was shown that tight selected PFO with $R = 0.7$ gives a better signal significance. Therefore the optimal choice of jet reconstruction for $\sqrt{s} = 3\,\text{TeV}$ is tight selected PFO with $R = 0.7$.

The extracted fitted parameters of optimal jet reconstructions are summarised in table 6.4.

6.4.2 Jet flavour tagging

Two b-jets out of six jets in final states are identified with flavour tagging processors. The processor calculates a set of discriminatively variables for a jet. After training the

(a)

(b)

(c)

(d)

(e)

(f)

Figure 6.3: figure 6.3a, 6.3c, and 6.3e show fitted mass of H_{bb}, H_{WW^*}, and W, respectively, for loose, normal and tight selected PFO against R parameter, with $\sqrt{s} = 3\,\text{TeV}$. figure 6.3b, 6.3d, and 6.3f show fitted combined widths divided by the fitted masses of H_{bb}, H_{WW^*}, and W, respectively, for loose, normal and tight selected PFO against R parameter, with $\sqrt{s} = 3\,\text{TeV}$.

(a) $\sqrt{s} = 1.4\,\mathrm{TeV}$ **(b)** $\sqrt{s} = 3\,\mathrm{TeV}$
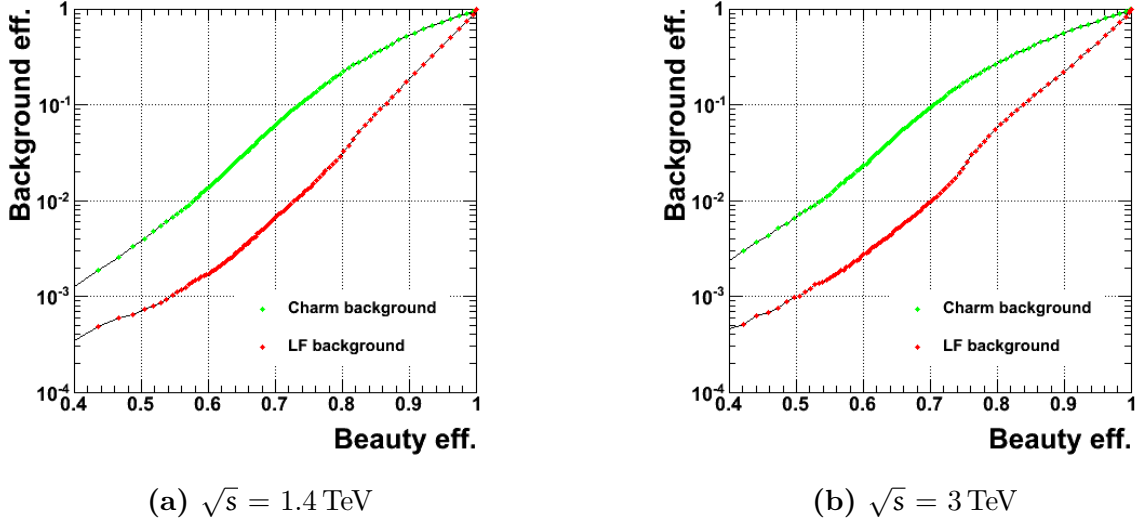
Figure 6.4: Performance of b-jet tagging with trainning samples

MVA, the MVA is applied to jets to produce a likelihood for b-jet and c-jet. For details see section **??**.

The existing LCFIPlus processor in Marlin package is used. The training sample of the flavour tagging processor is $\mathrm{e^-e^+ \to Z\nu\overline{\nu}}$, where Z decays to $\mathrm{q_l\overline{q}_l}$, $\mathrm{b\overline{b}}$, or $\mathrm{c\overline{c}}$ at $\sqrt{s} = 1.4\,\mathrm{TeV}$ and $\sqrt{s} = 3\,\mathrm{TeV}$, because they have similar event topology as the signal, and they have only two jets in the final state.

The selection efficiency of b-jets and c-jets with trainning samples are shown in figure **??**. Flavour tagging performs better at low energy. Because at high energy, particles at more collimated and more difficult to separate.

6.4.3 Jet pairing

The jet pairing was performed by seaking combination of jets that are compatible with signal $\mathrm{HH \to b\overline{b}W^+W^-}$.

The actual pairing is done via a minimisation

$$\chi^2 = \left(\frac{m_{ij} - \mu_{H_{bb}}}{\sigma'_{H_{bb}}}\right)^2 + \left(\frac{m_{klmn} - \mu_{H_{WW^*}}}{\sigma'_{H_{WW^*}}}\right)^2 + \left(\frac{m_{kl} - \mu_W}{\sigma'_W}\right)^2, \qquad (6.6)$$

where, $\mu_{H_{bb}}$ and $\sigma'_{H_{bb}}$ are the fitted invariant mass, and the fitted width, respectively. Both are obtained in section 6.4.1. $\sigma'_{H_{bb}}$ is $\sigma_{L,H_{bb}}$ when $m_{ij} < m_{H_{bb}}$, and $\sigma_{R,H_{bb}}$ otherwise. Similarly $\mu_{H_{WW^*}}$ and μ_W are fitted mass, and $\sigma'_{H_{WW^*}}$ and σ'_W are fitted invariant mass, and the fitted width, respectively. Out of the six jets from the jet clustering, indicated by subscript i, j, k, l, m, n, two are used for H_{bb}, two for W and four for H_{WW^*}. The fitted parameters used are listed in table 6.4. Additional requirement is that at least one of two jets forming H_{bb} needs to have a b-jet tag of 0.2 or greater.

With the χ^2, all possible combinations are tested, and the one with smallest χ^2 is chosen.

6.5 Pre-selection

Discriminative variables were calculated. Some are used as to discard background events, whilst hurting the signal events a bit. This allows MVA to concentrate on events where it is difficult to separate in a single parameter space.

6.5.1 Discriminative pre-selection cuts

As discussed before, events with identified leptons are rejected. Jet pairing implies that events with the largest b-jet tag less than 0.2 are rejected.

For $\sqrt{s} = 1.4\,\text{TeV}$, a range of variables were tested and three where chosen as pre-selection cuts.

Event with invariant mass of two higgs less than $150\,\text{GeV}$ is rejected. The cut above $120\,\text{GeV}$ is needed as some background samples were generated only for invariant mass greater than $120\,\text{GeV}$. Shown in table **??** and figure **??**, this cut is effective against samples with two quark final states.

Event with second highest b-jet tag less than 0.2 is rejected. This stricter cut than the jet pairing helps to reduce samples with no b-jets.

Event with p_T of two higgs less than $30\,\text{GeV}$ is rejected. This is extremely effective against samples with no neutrinos in the final state.

For $\sqrt{s} = 3\,\text{TeV}$, event with invariant mass of two higgs less than $150\,\text{GeV}$ is rejected, for the reason similar to $\sqrt{s} = 1.4\,\text{TeV}$.
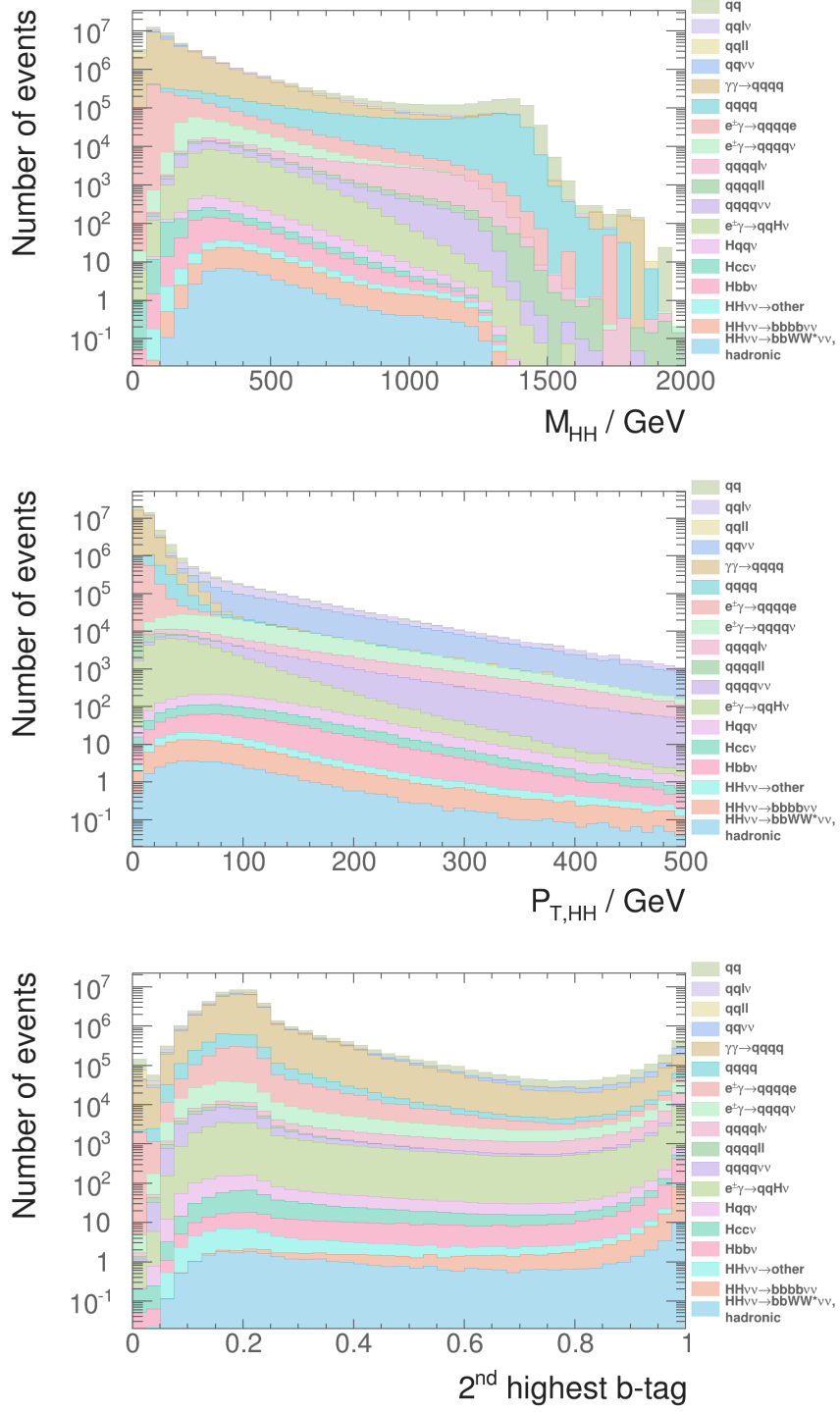
Figure 6.5: Discriminative pre-selection variables for $\sqrt{s} = 1.4\,\text{TeV}$, after rejecting events with identified leptons, and jet pairing
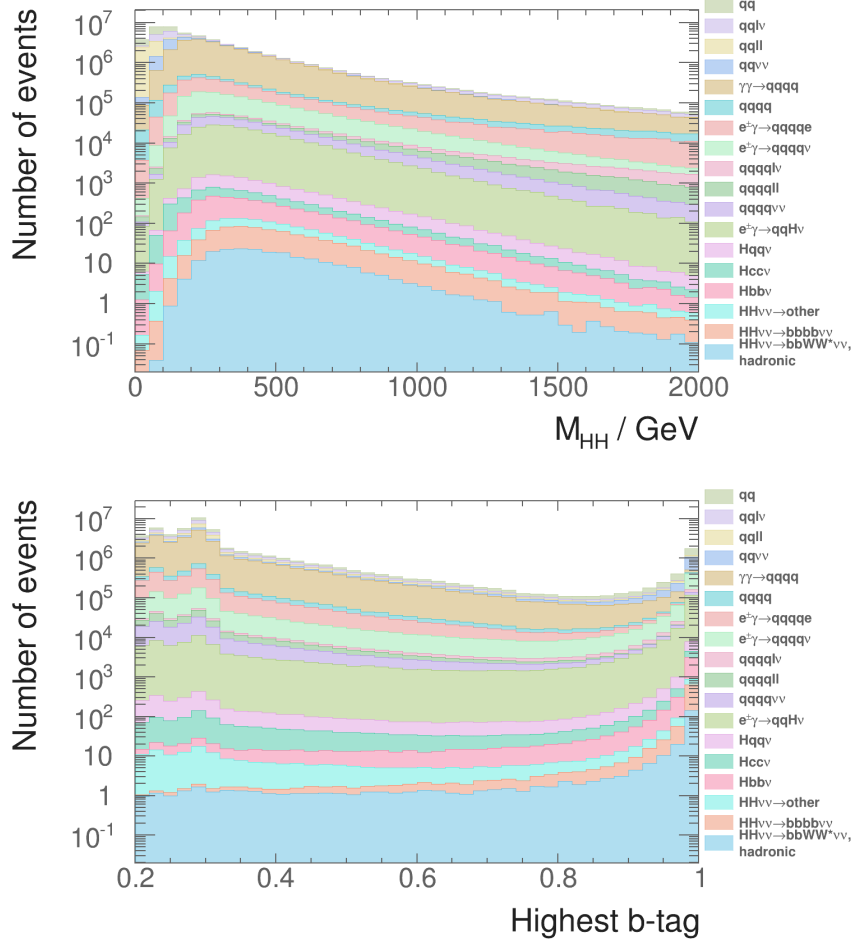
Figure 6.6: Discriminative pre-selection variables for $\sqrt{s} = 3\,\text{TeV}$, after rejecting events with identified leptons, and jet pairing

In addition, event with highest b-jet tag less than 0.7 is rejected. It is found that b-jet tag is less efficient at a higher $\sqrt{s}$. Therefore, a stricter cut at b-jet tag is useful to compensate for the tagging efficiency loss.

These set of cuts are stricter than usual analysis. The cross sections of signal channel for both $\sqrt{s}$ are extremely small, comparing to the background. Hence only the signal events with very clear characteristic topologies would be able to pass the final selection, in order to achieve a decent signal-to-background ratio. Therefore, a strict pre-selection cut would not hurt the final signal selection. On the contrary, final signal selection would benefit from MVA being able to focus the difficult background events, where their topologies are too similar to the signal events to separate in any single parameter space.

Channel / Efficiency $\sqrt{s} = 1.4\,\text{TeV}$	Expected number of events	Lepton ID and jet pairing	$m_{HH} > 150\,\text{GeV}$	$B_2 > 0.2$	$p_T > 30\,\text{GeV}$
$e^-e^+ \to HH\nu\overline{\nu} \to$ $b\overline{b}W^+W^-\nu\overline{\nu}$, hadronic	27.9	85.8%	85.6%	73.7%	66.4%
$e^-e^+ \to HH\nu\overline{\nu} \to$ $b\overline{b}b\overline{b}\nu\overline{\nu}$	67.6	90.8%	90.5%	90.1%	80.6%
$e^-e^+ \to HH\nu\overline{\nu} \to$ other	128.0	36.2%	35.3%	27.7%	24.7%
$e^-e^+ \to q_l q_l H\nu\overline{\nu}$	1304.0	60.7%	59.8%	44.9%	42.0%
$e^-e^+ \to c\overline{c}H\nu\overline{\nu}$	546.1	67.4%	57.7%	46.5%	43.4%
$e^-e^+ \to b\overline{b}H\nu\overline{\nu}$	463.0	73.9%	72.6%	68.7%	64.2%
$e^-e^+ \to qqqq$	1867650.0	48.8%	46.1%	17.3%	4.7%
$e^-e^+ \to qqqq\ell\ell$	93150.0	5.0%	4.9%	1.5%	0.3%
$e^-e^+ \to qqqq\ell\nu$	165600.0	15.1%	15.1%	12.4%	11.4%
$e^-e^+ \to qqqq\nu\overline{\nu}$	34800.0	50.7%	50.0%	20.1%	18.8%
$e^-e^+ \to qq$	6014250.0	54.5%	17.5%	8.4%	2.2%
$e^-e^+ \to qq\ell\nu$	6464550.0	14.1%	5.3%	2.0%	1.6%
$e^-e^+ \to qq\ell\ell$	4088700.0	13.0%	1.1%	0.6%	0.1%
$e^-e^+ \to qq\nu\nu$	1181550.0	60.1%	12.3%	6.2%	5.8%
$e^-\gamma(BS) \to e^- qqqq$	1305787.5	23.3%	10.6%	4.4%	0.4%
$e^+\gamma(BS) \to e^+ qqqq$	1300837.5	23.4%	10.5%	4.3%	0.4%
$e^-\gamma(EPA) \to e^- qqqq$	430650.0	11.1%	5.4%	2.2%	0.3%
$e^+\gamma(EPA) \to e^+ qqqq$	430350.0	11.1%	5.3%	2.1%	0.3%
$e^-\gamma(BS) \to \nu qqqq$	89775.0	58.3%	56.8%	31.0%	27.7%
$e^+\gamma(BS) \to \overline{\nu} qqqq$	89212.5	57.6%	56.1%	30.3%	27.3%
$e^-\gamma(EPA) \to \nu qqqq$	26100.0	29.6%	28.9%	15.4%	13.9%
$e^+\gamma(EPA) \to \overline{\nu} qqqq$	25950.0	29.2%	28.5%	15.0%	13.7%
$e^-\gamma(BS) \to qqH\nu$	17775	61.0%	59.8%	45.5%	34.6%
$e^+\gamma(BS) \to qqH\nu$	17662.5	61.1%	60.0%	45.6%	34.6%
$e^-\gamma(EPA) \to qqH\nu$	5085	31.8%	31.2%	23.7%	18.2%
$e^+\gamma(EPA) \to qqH\nu$	5085	31.9%	31.3%	23.8%	18.4%
$\gamma(BS)\gamma(BS) \to qqqq$	2054951.5	56.3%	23.9%	9.6%	0.3%
$\gamma(BS)\gamma(EPA) \to qqqq$	4521037.5	33.6%	14.2%	5.7%	0.4%
$\gamma(EPA)\gamma(BS) \to qqqq$	4539150.0	33.7%	14.2%	5.7%	0.4%
$\gamma(EPA)\gamma(EPA) \to qqqq$	1129500.0	21.1%	9.1%	3.7%	0.4%

Table 6.5: List of signal and background samples with the corresponding expected number at $\sqrt{s} = 1.4\,\text{TeV}$, assuming a luminosity of 1500fb^{-1}. The selection efficiencies are presented in a "flow" fashion, as the every selection cut contains all the cuts to the left of it.

Channel / Efficiency $\sqrt{s} = 3\,\mathrm{TeV}$	Expected number of events	Lepton ID and jet pairing	$m_{HH} > 150\,\mathrm{GeV}$	$B_1 > 0.7$
$e^-e^+ \to HH\nu\bar{\nu} \to$ $b\bar{b}W^+W^-\nu\bar{\nu}$, hadronic	146.0	80.2%	79.9%	69.7%
$e^-e^+ \to HH\nu\bar{\nu} \to$ $b\bar{b}b\bar{b}\nu\bar{\nu}$	355.0	83.4%	82.9%	81.2%
$e^-e^+ \to HH\nu\bar{\nu} \to$ other	675.0	36.7%	35.8%	25.2%
$e^-e^+ \to q_l q_l H\nu\bar{\nu}$	6115.4	59.5%	58.5%	40.4%
$e^-e^+ \to c\bar{c}H\nu\bar{\nu}$	2249.9	64.8%	58.4%	39.3%
$e^-e^+ \to b\bar{b}H\nu\bar{\nu}$	2197.7	69.7%	68.4%	64.2%
$e^-e^+ \to qqqq$	1093000.0	48.5%	39.7%	3.0%
$e^-e^+ \to qqqq\ell\ell$	338600.0	14.7%	14.2%	0.7%
$e^-e^+ \to qqqq\ell\nu$	213200.0	19.7%	19.4%	10.0%
$e^-e^+ \to qqqq\nu\bar{\nu}$	143000.0	58.4%	57.3%	11.9%
$e^-e^+ \to qq$	5897800.0	62.8%	13.2%	2.7%
$e^-e^+ \to qq\ell\nu$	11121800	28.3%	11.9%	0.3%
$e^-e^+ \to qq\ell\ell$	6639200.0	38.3%	2.9%	0.7%
$e^-e^+ \to qq\nu\nu$	2635000.0	71.4%	24.1%	5.3%
$e^-\gamma(BS) \to e^- qqqq$	2004388.1	23.3%	21.5%	0.8%
$e^+\gamma(BS) \to e^+ qqqq$	2002334.1	23.4%	21.6%	0.8%
$e^-\gamma(EPA) \to e^- qqqq$	575600.0	12.0%	11.0%	0.5%
$e^+\gamma(EPA) \to e^+ qqqq$	575600.0	12.0%	10.9%	0.4%
$e^-\gamma(BS) \to \nu qqqq$	414750.0	61.7%	59.5%	20.4%
$e^+\gamma(BS) \to \bar{\nu} qqqq$	414434.0	61.2%	59.1%	19.4%
$e^-\gamma(EPA) \to \nu qqqq$	108400.0	30.9%	29.9%	9.6%
$e^+\gamma(EPA) \to \bar{\nu} qqqq$	108400.0	30.7%	29.7%	9.1%
$e^-\gamma(BS) \to qqH\nu$	92588.0	58.3%	56.2%	37.3%
$e^+\gamma(BS) \to qqH\nu$	92430.0	58.1%	56.0%	37.1%
$e^-\gamma(EPA) \to qqH\nu$	23400.0	30.1%	29.2%	19.4%
$e^+\gamma(EPA) \to qqH\nu$	23400.0	29.7%	28.6%	18.8%
$\gamma(BS)\gamma(BS) \to qqqq$	18009413.9	54.2%	49.2%	1.9%
$\gamma(BS)\gamma(EPA) \to qqqq$	3824548.1	33.5%	30.2%	1.2%
$\gamma(EPA)\gamma(BS) \to qqqq$	3828498.1	33.7%	30.3%	1.2%
$\gamma(EPA)\gamma(EPA) \to qqqq$	805400.0	22.0%	19.8%	0.8%

Table 6.6: List of signal and background samples with the corresponding expected number at $\sqrt{s} = 3\,\mathrm{TeV}$, assuming a luminosity of $2000\mathrm{fb}^{-1}$. The selection efficiencies are presented in a "flow" fashion, as the every selection cut contains all the cuts to the left of it.

6.5.2 Sanity cuts

A set of very loose cuts, aiming to reduce the range of some discriminative variables to increase the effectiveness of MVA. (See section **??** on MVA) These cuts are very loose and physics motivated.

For $\sqrt{s} = 1.4\,\text{TeV}$, invariant masses for H_{bb}, H_{WW^*}, W, and HH are smaller than 500, 800, 200, and 1400 GeV, respectively.

For $\sqrt{s} = 3\,\text{TeV}$, invariant masses for H_{bb}, H_{WW^*}, W, and HH are smaller than 500, 800, 200, and 3000 GeV, respectively.

The selection efficiencies after sanity cuts and other pre-selection cuts stated above, are listed in table **??**.

6.5.3 Mutually exclusive cuts for $HH \rightarrow b\overline{b}W^+W^-$ and $HH \rightarrow b\overline{b}b\overline{b}$

Since the analysis for $e^-e^+ \rightarrow HH\nu\overline{\nu}$ channel is divided into two subchannels, $HH \rightarrow b\overline{b}W^+W^- \rightarrow b\overline{b}qqqq$ and $HH \rightarrow b\overline{b}b\overline{b}$, it is convenient to divided samples, both signal and background, into two mutually exclusive sets. This will make combining subchaneels much easier, as correlations between subchannels do not need to be considered.

The most distinctive difference between two subchannels, is that they have different number of jets, and different number of b-jets in the final state. So variables related to number of b-jets or a number of jets are suitable for separating two subchannels.

Shown in figure 6.7, two subchannels can be clearly separated in the two dimensional parameter space. The optimal rectangular cuts were selected by scanning the two parameters, and maximising

$$\varepsilon = \mathsf{P}(\mathsf{subchannel}_1|\mathsf{selection}) \times \mathsf{P}(\mathsf{subchannel}_2|\neg\mathsf{selection}) \qquad (6.7)$$

where $\mathsf{selection}$ represents the mutually exclusive cuts, $\neg\mathsf{selection}$ indicates the phase space not covered by the $\mathsf{selection}$.

Variables tested includes ΣB_{4jets}, $\sum_1^3 B_{4jets}$, y_{34}, y_{45}, y_{56}, y_{67} and other related variables. The best separation was summarised in table 6.7.
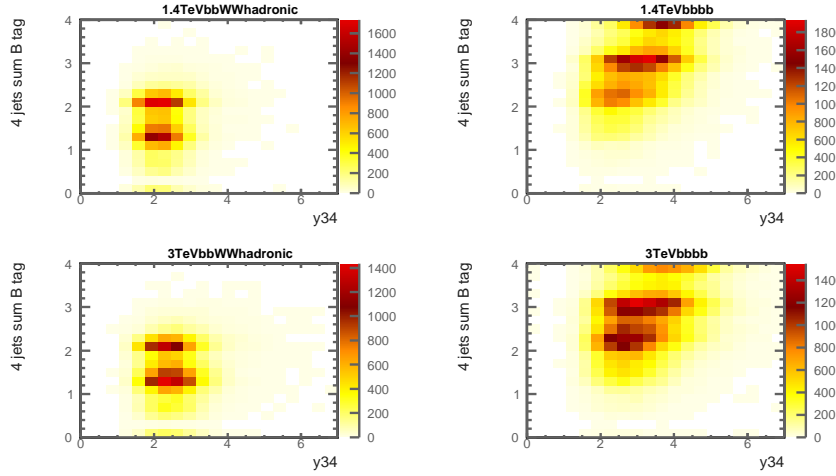
Figure 6.7: Sum of b tag against y_{34}, shown for signal samples

$\sqrt{s}$	selection	$HH \to b\bar{b}qqqq$ Selection Efficiency	$HH \to b\bar{b}b\bar{b}$ Selection Efficiency
1.4 TeV	$\Sigma B_{4jets} < 2.3$ and $y_{34} < 3.7$	86%	78%
3 TeV	$\Sigma B_{4jets} < 2.3$ and $y_{34} < 3.6$	89%	82%

Table 6.7: Mutually exclusive cuts, for full signal samples

The selection efficiencies after mutually exclusive cuts and other pre-selection cuts stated above, are listed in table **??**.

6.6 Discriminative Variables

A series of discriminative variables were calculated, and fed into MVA for signal selection.

The full list of variables can be found in table **??**. Same set of variables are used for $\sqrt{s} = 1.4\,\text{TeV}$ and $\sqrt{s} = 3\,\text{TeV}$.

figure **??** hows the the variable XX which gives a good discrimination of signal against background.

The optimal set were chosen to give the best MVA performance, whilst no strong pair-wise correlation between any two variables, shown in figure **??**.

Channel / Efficiency	Sanity $\sqrt{s}$ = 1.4 TeV	Mutually exclusive $\sqrt{s}$ = 1.4 TeV	Sanity $\sqrt{s}$ = 3 TeV	Mutually exclusive $\sqrt{s}$ = 3 TeV
$e^-e^+ \to HH\nu\bar{\nu} \to$ $b\bar{b}W^+W^-\nu\bar{\nu}$, hadronic	66.4%	59.7%	69.5%	61.7%
$e^-e^+ \to HH\nu\bar{\nu} \to$ $b\bar{b}b\bar{b}\nu\bar{\nu}$	80.6%	15.4%	81.1%	18.8%
$e^-e^+ \to HH\nu\bar{\nu} \to$ other	24.7%	20.5%	25.1%	20.0%
$e^-e^+ \to q_l q_l H\nu\bar{\nu}$	42.0%	39.5%	40.3%	35.9%
$e^-e^+ \to c\bar{c}H\nu\bar{\nu}$	43.4%	31.7%	39.2%	26.2%
$e^-e^+ \to b\bar{b}H\nu\bar{\nu}$	64.2%	25.2%	64.2%	25.9%
$e^-e^+ \to qqqq$	4.6%	3.4%	2.5%	1.4%
$e^-e^+ \to qqqq\ell\ell$	3.3%	3.1%	0.7%	0.6%
$e^-e^+ \to qqqq\ell\nu$	11.4%.	9.8%	9.2%	7.2%
$e^-e^+ \to qqqq\nu\bar{\nu}$	18.8%	16.6%	11.8%	9.0%
$e^-e^+ \to qq$	2.0%	0.8%	2.5%	1.4%
$e^-e^+ \to qq\ell\nu$	1.6%	0.9%	0.3%	0.1%
$e^-e^+ \to qq\ell\ell$	0.1%	0.1%	0.7%	0.4%
$e^-e^+ \to qq\nu\nu$	5.8%	4.0%	5.3%	3.1%
$e^-\gamma(BS) \to e^-qqqq$	0.4%	0.3%	0.8%	0.7%
$e^+\gamma(BS) \to e^+qqqq$	0.4%	0.4%	0.8%	0.7%
$e^-\gamma(EPA) \to e^-qqqq$	0.3%	0.2%	0.4%	0.4%
$e^+\gamma(EPA) \to e^+qqqq$	0.3%	0.3%	0.4%	0.3%
$e^-\gamma(BS) \to \nu qqqq$	27.7%	25.3%	20.3%	16.8%
$e^+\gamma(BS) \to \bar{\nu}qqqq$	27.3%	24.9%	19.3%	15.9%
$e^-\gamma(EPA) \to \nu qqqq$	13.9%	12.6%	9.4%	7.8%
$e^+\gamma(EPA) \to \bar{\nu}qqqq$	13.7%	12.3%	8.9%	7.3%
$e^-\gamma(BS) \to qqH\nu$	34.6%	30.6%	37.2%	30.2%
$e^+\gamma(BS) \to qqH\nu$	34.6%	30.6%	37.1%	30.2%
$e^-\gamma(EPA) \to qqH\nu$	18.2%	16.0%	19.0%	15.7%
$e^+\gamma(EPA) \to qqH\nu$	18.4%	16.1%	18.4%	15.2%
$\gamma(BS)\gamma(BS) \to qqqq$	0.3%	0.3%	1.9%	1.7%
$\gamma(BS)\gamma(EPA) \to qqqq$	0.4%	0.3%	1.1%	1.0%
$\gamma(EPA)\gamma(BS) \to qqqq$	0.4%	0.3%	1.1%	1.0%
$\gamma(EPA)\gamma(EPA) \to qqqq$	0.4%	0.3%	0.7%	0.6%

Table 6.8: List of signal and background samples with the corresponding expected number at $\sqrt{s} = 1.4$ TeV and $\sqrt{s} = 3$ TeV, assuming a luminosity of 1500 and 2000fb^{-1}, respectively. The selection efficiencies are presented in a "flow" fashion, as the every selection cut contains all the cuts to the left of it.

Variable	Description
$m_{H_{bb}}$	Invariant mass of H_{bb}
$m_{H_{WW^*}}$	Invariant mass of H_{WW^*}
m_W	Invariant mass of W
m_{HH}	Invariant mass of HH
E_{W^*}	Energy of W^*
E_{mis}	Missing energy, assuming collision at $\sqrt{s}$
$p_{TH_{bb}}$	Transverse momentum of H_{bb}
$p_{TH_{WW^*}}$	Transverse momentum of H_{WW^*}
p_{THH}	Transverse momentum of HH
η_{mis}	Pseudorapidity of missing momentum, assuming collision at $\sqrt{s}$
p_{THH}	Transverse momentum of HH
$-\ln(y_{23})$	minus ln of y_{23}. See section **??** for y parameter. See section **??** for the ln transformation
$-\ln(y_{34})$	minus ln of y_{34}.
$-\ln(y_{45})$	minus ln of y_{45}.
$-\ln(y_{56})$	minus ln of y_{56}.
$B_{1,H_{bb}}$	Highest b-jet tag value of two jets forming H_{bb}.
$B_{2,H_{bb}}$	Lowest b-jet tag value of two jets forming H_{bb}.
$B_{1,W}$	Highest b-jet tag value of two jets forming W.
B_{1,W^*}	Highest b-jet tag value of two jets forming W^* .
$C_{1,H_{bb}}$	Highest c-jet tag value of two jets forming H_{bb}.
$C_{1,W}$	Highest c-jet tag value of two jets forming W.
$\lvert S \rvert$	Modulus of sphericity, S. See section **??**.
$acol_{H_{bb}}$	Acolinearity of two jets forming H_{bb}.
$acol_W$	Acolinearity of two jets forming W.
$acol_{HH}$	Acolinearity of H_{bb} and H_{WW^*}.
$N_{H_{bb}}$	Number of PFOs forming H_{bb}.
$N_{H_{WW^*}}$	Number of PFOs forming H_{WW^*}.
N_W	Number of PFOs forming W.
N_{W^*}	Number of PFOs forming W^*.
$\cos\left(\theta^*_{H_{bb}}\right)$	Cosine of opening angles of two jets forming H_{bb}, in their rest frame.
$\cos\left(\theta^*_{H_{WW^*}}\right)$	Cosine of opening angles of W and W^*, forming H_{WW^*}, in their rest frame.
$\cos\left(\theta^*_W\right)$	Cosine of opening angles of two jets forming W, in their rest frame.

6.7 Multivariate analysis

Multivariate analysis was performed with TMVA package. The classifier that performs the best was found to be the boosted decision tree. See section **??** for details on boosted decision tree.

The parameters for boosted decision tree were optimised and checked for overtraining. The most important variables are the depth of the tree and the number of trees. Other parameters includes the minimum number of nodes in a leaf, the number of cuts of a variable, the learning rate, the sampling fraction, the yes/no or purity leaf, adaBoost or gradient boost.

The optimisation and overtraining test was done with $\sqrt{s} = 3\,\text{TeV}$ samples. $\sqrt{s} = 1.4\,\text{TeV}$ samples produce similar results.

Half of the samples were used for training, and the other half used for testing.

6.8 Signal selection results

6.9 Couplings extration

Channel / Efficiency $\sqrt{s} = 1.4\,\text{TeV}$	Expected number of events	Pre-selection efficiency	MVA efficiency	Number of events after MVA
$e^-e^+ \to HH\nu\bar{\nu} \to$ $b\bar{b}W^+W^-\nu\bar{\nu}$, hadronic	27.9	59.8%	8.2%	1.37
$e^-e^+ \to HH\nu\bar{\nu} \to$ $b\bar{b}b\bar{b}\nu\bar{\nu}$	67.6	15.4%	0.5%	0.05
$e^-e^+ \to HH\nu\bar{\nu} \to$ other	128.0	20.4%	1.7%	0.45
$e^-e^+ \to q_l q_l H\nu\bar{\nu}$	1304.0	39.5%	0.05%	0.29
$e^-e^+ \to c\bar{c}H\nu\bar{\nu}$	546.1	31.6%	0.1%	0.16
$e^-e^+ \to b\bar{b}H\nu\bar{\nu}$	463.0	24.7%	0.3%	0.37
$e^-e^+ \to qqqq$	1867650.0	3.3%	-	-
$e^-e^+ \to qqqq\ell\ell$	93150.0	0.3%	-	-
$e^-e^+ \to qqqq\ell\nu$	165600.0	9.8%	0.01%	2.06
$e^-e^+ \to qqqq\nu\bar{\nu}$	34800.0	16.5%	0.002%	0.10
$e^-e^+ \to qq$	6014250.0	0.8%	-	-
$e^-e^+ \to qq\ell\nu$	6464550.0	0.9%	-	-
$e^-e^+ \to qq\ell\ell$	4088700.0	0.08%	-	-
$e^-e^+ \to qq\nu\nu$	1181550.0	4.0%	-	-
$e^-\gamma(\text{BS}) \to e^- qqqq$	1305787.5	0.3%	-	-
$e^+\gamma(\text{BS}) \to e^+ qqqq$	1300837.5	0.4%	-	-
$e^-\gamma(\text{EPA}) \to e^- qqqq$	430650.0	0.3%	-	-
$e^+\gamma(\text{EPA}) \to e^+ qqqq$	430350.0	0.3%	-	-
$e^-\gamma(\text{BS}) \to \nu qqqq$	89775.0	25.4%	0.005%	1.09
$e^+\gamma(\text{BS}) \to \bar{\nu} qqqq$	89212.5	24.9%	0.004%	0.96
$e^-\gamma(\text{EPA}) \to \nu qqqq$	26100.0	12.6%	-	-
$e^+\gamma(\text{EPA}) \to \bar{\nu} qqqq$	25950.0	12.4%	0.008%	0.27
$e^-\gamma(\text{BS}) \to qqH\nu$	17775	30.8%	0.02%	1.00
$e^+\gamma(\text{BS}) \to qqH\nu$	17662.5	30.6%	0.02%	1.16
$e^-\gamma(\text{EPA}) \to qqH\nu$	5085	16.0%	0.04%	0.33
$e^+\gamma(\text{EPA}) \to qqH\nu$	5085	16.2%	0.08%	0.62
$\gamma(\text{BS})\gamma(\text{BS}) \to qqqq$	2054951.5	0.2%	-	-
$\gamma(\text{BS})\gamma(\text{EPA}) \to qqqq$	4521037.5	0.4%	-	-
$\gamma(\text{EPA})\gamma(\text{BS}) \to qqqq$	4539150.0	0.3%	-	-
$\gamma(\text{EPA})\gamma(\text{EPA}) \to qqqq$	1129500.0	0.3%	-	-

Table 6.10: List of signal and background samples with the corresponding expected number at $\sqrt{s} = 1.4\,\text{TeV}$, for a luminosity of 1500fb^{-1}. The number of events, selection efficiency of pre-selection, selection efficiency of MVA after pre-selection, number of events after MVA are shown. - represents no events passing the MVA.

Channel / Efficiency $\sqrt{s} = 3$ TeV	Expected number of events	Pre-selection efficiency	MVA efficiency	Number of events after MVA
$e^-e^+ \to HH\nu\overline{\nu} \to$ $b\overline{b}W^+W^-\nu\overline{\nu}$, hadronic	146.0	61.7%	11.6%	10.43
$e^-e^+ \to HH\nu\overline{\nu} \to$ $b\overline{b}b\overline{b}\nu\overline{\nu}$	355.0	18.8%	1.5%	1.01
$e^-e^+ \to HH\nu\overline{\nu} \to$ other	675.0	20.0%	3.6%	4.93
$e^-e^+ \to q_l q_l H\nu\overline{\nu}$	6115.4	36.0%	0.4%	9.42
$e^-e^+ \to c\overline{c}H\nu\overline{\nu}$	2249.9	26.3%	0.5%	3.13
$e^-e^+ \to b\overline{b}H\nu\overline{\nu}$	2197.7	25.8%	1.2%	6.82
$e^-e^+ \to qqqq$	1093000.0	1.4%	0.01%	1.43
$e^-e^+ \to qqqq\ell\ell$	338600.0	0.6%	-	-
$e^-e^+ \to qqqq\ell\nu$	213200.0	7.3%	0.05%	8.35
$e^-e^+ \to qqqq\nu\overline{\nu}$	143000.0	9.0%	0.05%	6.35
$e^-e^+ \to qq$	5897800.0	1.4%	-	-
$e^-e^+ \to qq\ell\nu$	11121800	0.1%	-	-
$e^-e^+ \to qq\ell\ell$	6639200.0	0.4%	-	-
$e^-e^+ \to qq\nu\nu$	2635000.0	3.1%	-	-
$e^-\gamma(BS) \to e^- qqqq$	2004388.1	0.7%	-	-
$e^+\gamma(BS) \to e^+ qqqq$	2002334.1	0.7%	-	-
$e^-\gamma(EPA) \to e^- qqqq$	575600.0	0.4%	-	-
$e^+\gamma(EPA) \to e^+ qqqq$	575600.0	0.3%	-	-
$e^-\gamma(BS) \to \nu qqqq$	414750.0	16.8%	0.04%	30.7
$e^+\gamma(BS) \to \overline{\nu} qqqq$	414434.0	15.9%	0.05%	30.3
$e^-\gamma(EPA) \to \nu qqqq$	108400.0	7.8%	0.04%	3.37
$e^+\gamma(EPA) \to \overline{\nu} qqqq$	108400.0	7.3%	0.03%	2.63
$e^-\gamma(BS) \to qqH\nu$	92588.0	30.2%	0.2%	67.5
$e^+\gamma(BS) \to qqH\nu$	92430.0	30.3%	0.2%	54.2
$e^-\gamma(EPA) \to qqH\nu$	23400.0	15.4%	0.2%	7.88
$e^+\gamma(EPA) \to qqH\nu$	23400.0	15.2%	0.3%	10.2
$\gamma(BS)\gamma(BS) \to qqqq$	18009413.9	1.6%	-	-
$\gamma(BS)\gamma(EPA) \to qqqq$	3824548.1	1.0%	-	-
$\gamma(EPA)\gamma(BS) \to qqqq$	3828498.1	1.0%	-	-
$\gamma(EPA)\gamma(EPA) \to qqqq$	805400.0	0.6%	-	-

Table 6.11: List of signal and background samples with the corresponding expected number at $\sqrt{s} = 3$ TeV, for a luminosity of 2000fb^{-1}. The number of events, selection efficiency of pre-selection, selection efficiency of MVA after pre-selection, number of events after MVA are shown. - represents no events passing the MVA.

Channel / Efficiency $\sqrt{s} = 3\,\mathrm{TeV}$	Expected number of events	Pre-selection efficiency	MVA efficiency	Number of events after MVA
$\mathrm{e^-e^+ \to HH\nu\bar{\nu} \to}$ $\mathrm{b\bar{b}W^+W^-\nu\bar{\nu}}$, semi-leptonic	96.8	44.6%	21.9%	9.48
$\mathrm{e^-e^+ \to HH\nu\bar{\nu} \to}$ $\mathrm{b\bar{b}b\bar{b}\nu\bar{\nu}}$	355.0	13.3%	10.9%	5.16
$\mathrm{e^-e^+ \to HH\nu\bar{\nu} \to}$ other	724.2	13.1%	13.6%	12.89
$\mathrm{e^-e^+ \to q_l q_l H\nu\bar{\nu}}$	6115.4	7.4%	13.7%	62.63
$\mathrm{e^-e^+ \to c\bar{c}H\nu\bar{\nu}}$	2249.9	6.3%	12.1%	17.10
$\mathrm{e^-e^+ \to b\bar{b}H\nu\bar{\nu}}$	2197.7	15.9%	5.1%	18.03
$\mathrm{e^-e^+ \to qqqq}$	1093000.0	0.6%	0.2%	15.04
$\mathrm{e^-e^+ \to qqqq\ell\ell}$	338600.0	1.0%	0.06%	1.85
$\mathrm{e^-e^+ \to qqqq\ell\nu}$	213200.0	27.6%	0.5%	270.33
$\mathrm{e^-e^+ \to qqqq\nu\bar{\nu}}$	143000.0	1.9%	1.6%	43.78
$\mathrm{e^-e^+ \to qq}$	5897800.0	0.4%	0.3%	60.82
$\mathrm{e^-e^+ \to qq\ell\nu}$	11121800	0.3%	0.08%	21.24
$\mathrm{e^-e^+ \to qq\ell\ell}$	6639200.0	0.6%	0.2%	84.14
$\mathrm{e^-e^+ \to qq\nu\nu}$	2635000.0	0.4%	0.9%	92.55
$\mathrm{e^-\gamma(BS) \to e^- qqqq}$	2004388.1	1.2%	-	-
$\mathrm{e^+\gamma(BS) \to e^+ qqqq}$	2002334.1	1.2%	-	-
$\mathrm{e^-\gamma(EPA) \to e^- qqqq}$	575600.0	1.1%	-	-
$\mathrm{e^+\gamma(EPA) \to e^+ qqqq}$	575600.0	1.1%	-	-
$\mathrm{e^-\gamma(BS) \to \nu qqqq}$	414750.0	3.7%	1.5%	226.77
$\mathrm{e^+\gamma(BS) \to \bar{\nu} qqqq}$	414434.0	3.5%	1.6%	225.68
$\mathrm{e^-\gamma(EPA) \to \nu qqqq}$	108400.0	11.2%	0.9%	107.90
$\mathrm{e^+\gamma(EPA) \to \bar{\nu} qqqq}$	108400.0	10.7%	0.8%	92.75
$\mathrm{e^-\gamma(BS) \to qqH\nu}$	92588.0	7.9%	10.7%	779.36
$\mathrm{e^+\gamma(BS) \to qqH\nu}$	92430.0	7.9%	10.1%	741.57
$\mathrm{e^-\gamma(EPA) \to qqH\nu}$	23400.0	22.9%	6.9%	369.52
$\mathrm{e^+\gamma(EPA) \to qqH\nu}$	23400.0	22.7%	7.2%	381.33
$\mathrm{\gamma(BS)\gamma(BS) \to qqqq}$	18009413.9	0.4%	-	-
$\mathrm{\gamma(BS)\gamma(EPA) \to qqqq}$	3824548.1	1.0%	-	-
$\mathrm{\gamma(EPA)\gamma(BS) \to qqqq}$	3828498.1	1.0%	0.08%	28.85
$\mathrm{\gamma(EPA)\gamma(EPA) \to qqqq}$	805400.0	1.1%	-	-

Table 6.12: List of signal and background samples with the corresponding expected number at $\sqrt{s} = 3\,\mathrm{TeV}$, for a luminosity of $2000\mathrm{fb}^{-1}$. The number of events, selection efficiency of pre-selection, selection efficiency of MVA after pre-selection, number of events after MVA are shown. - represents no events passing the MVA.

Colophon

This thesis was made in LaTeX 2$_\varepsilon$ using the "hepthesis" class [13].

Bibliography

[1] F. Gaede, Nucl. Instrum. Meth. **A559**, 177 (2006).

[2] J. S. Marshall, A. MÍźnnich, and M. A. Thomson, Nucl. Instrum. Meth. **A700**, 153 (2013), 1209.4039.

[3] W. Kilian, T. Ohl, and J. Reuter, European Physical Journal C **71** (2011).

[4] T. Sjostrand, (1995), hep-ph/9508391.

[5] S. Jadach, Z. Was, R. Decker, and J. H. Kuhn, Comput. Phys. Commun. **76**, 361 (1993).

[6] P. Mora de Freitas and H. Videau, p. 623 (2002).

[7] GEANT4, S. Agostinelli *et al.*, Nucl.Instrum.Meth. **A506**, 250 (2003).

[8] F. Gaede and J. Engels, EUDET Report (2007).

[9] J. S. Marshall and M. A. Thomson, Eur. Phys. J. **C75**, 439 (2015), 1506.05348.

[10] B. Xu, Improvement of photon reconstruction in PandoraPFA, in *Proceedings, International Workshop on Future Linear Colliders (LCWS15): Whistler, B.C., Canada, November 02-06, 2015*, 2016, 1603.00013.

[11] Particle Data Group, K. A. Olive *et al.*, Chin. Phys. **C38**, 090001 (2014).

[12] A. MÍźnnich, CERN Report No. LCD-Note-2010-009, 2010 (unpublished).

[13] A. Buckley, The hepthesis LaTeX class.

List of figures

List of tables